Micromechanics-based elasto-plastic-damage energy formulation for strain gradient solids with granular microstructure

Luca Placidi (1), Emilio Barchiesi (2,3), Anil Misra (4), Dmitry Timofeev (2),

April 26, 2021

(1) International Telematic University UNINETTUNO. Faculty of Engineering. Corso Vittorio Emanuele II 39 00186, Roma (Italy). Corresponding: *luca.placidi@uninettunouniversity.net.*

(2) International Research Center on Mathematics and Mechanics of Complex Systems (M&MoCS). Università degli Studi dell'Aquila. Via Giovanni Gronchi 18 - Zona industriale di Pile 67100, L'Aquila (Italy).

(3) École Nationale d'Ingénieurs de Brest, 760 ENIB, UMR CNRS 6027, IRDL, F-29200 Brest, France

(4) The University of Kansas. Civil, Environmental and Architectural Engineering Department. 1530 W. 15th Street, Lawrence, KS 66045-7609.

Abstract

This paper is devoted to the development of a continuum theory for materials having granular microstructure and accounting for some dissipative phenomena like damage and plasticity. The continuum description is constructed by means of purely mechanical concepts, assuming expressions of elastic and dissipation energies as well as postulating a hemi-variational principle, without incorporating any additional postulate like flow rules. Granular micromechanics is connected kinematically to the continuum scale through Piola's ansatz. Mechanically meaningful objective kinematic descriptors aimed at accounting for grain-grain relative displacements in finite deformations are proposed. Karush-Kuhn-Tucker (KKT) type conditions, providing evolution equations for damage and plastic variables associated to grain-grain interactions, are derived solely from the fundamental postulates. Numerical experiments have been performed to investigate the applicability of the model. Cyclic loading-unloading histories have been considered to elucidate the material-hysteretic features of the continuum, which emerge from simple grain-grain interactions. We also assess the competition between damage and plasticity, each having an effect on the other. Further, the evolution of the load-free shape is shown not only to assess the plastic behavior, but also to make tangible the point that, in the proposed approach, plastic strain is found to be intrinsically compatible with the existence of a placement function.

1 Introduction

Approaches aimed at handling dissipation occurring in non-conservative physical systems are extensively discussed in the scientific literature [15, 20, 28, 26, ?]. Damage and plasticity are complex dissipative phenomena which are especially interesting for the engineering community, because they are occurring in many different materials employed in engineering applications [29, 30, 50], like structural steel, and concrete. Clearly, the detailed description of these phenomena faces serious challenges, especially for complex material systems exhibiting, as an instance, lattice-type [45, 18, 33] or granular [29, 31] microstructure. In the last years, continuum approaches to damage [1, 4] and plasticity [11, 5, 16, ?, 17, 23, 29, 30, 40, 41] modeling have been vigorously pursued, including the development of phase field models [6, 7, 8, 44, 25, 24] for shearing bands and fracture analyses. Besides phenomenological approaches, many multi-scale approaches [19, ?, ?], linking low-scale descriptions with the continuum one, have also been proposed [10, 22]

to incorporate complex emerging behaviors within the continuum. We here exploit a methodology for developing continuum models of granular material systems which incorporates many of the characteristic features of granular microstructures, which are collectively termed as micro-mechano-morphology.

Except for living tissues and purposely designed meta-materials having the capacity to self-heal [13, ?, ?, 21], materials which are usually employed in engineering applications cannot reverse autonomously their damaged state if only subjected to loading. This is generally accounted for by the rate in time of damage variables being required to be positive. Clearly, also plastic deformations entail irreversible phenomena, which at continuum scale reflects in an irreversible change of the load-free configuration [23, 40, 41]. This is usually taken into account with the use of so-called plastic multipliers that, as damage variables, can only increase their value in time. Following these ideas, we encode non-reversibility by treating plastic multipliers and damage variables as monotonically time-varying kinematic descriptors [46] in dealing with the mechanical description of damaging solids with granular microstructure undergoing both elastic and plastic deformations. As widely discussed in previous works, the deformation of such materials can be effectively described in a coarse-grained fashion by means of the relative movements of interacting grains' centroids/barycenters, regardless of the actual deformation distribution within the grains. Therefore, in a coarse-grained description, the deformation energy of a material with granular microstructure can be expressed in terms of these relative movements. The quantification of the energy dissipated because of damage and/or plasticity can be addressed similarly, without taking care of the actual sub-granular mechanisms. The volumetric deformation energy, i.e. the deformation energy of a unit material volume, can thus be obtained as the aggregation of deformation energies associated to grain-grain interactions occurring within the unit material volume. Mathematically, in the continuum limit, this aggregation consists into the infinite sum of the deformation energies associated to grain-grain interactions, being these last identified by their orientation in space. This view has proved to be a promising approach for the description of granular systems, both at discrete and continuum levels [2, 3, 12, 27, 31, 47, 48, 49, ?]. With this view as point of departure, we here utilize a variational approach [14, ?]. At first, we construct an objective and reversible kinematic variable for measuring grain-grain relative displacements. As we make use of the continuum-scale strain, as well as of its spatial gradient, such a kinematic variable can be easily linked to the placement function of the continuum.

As done customarily in granular micromechanics (see for example [39, 29]), we decompose the objective grain-grain relative displacement into a component along the vector joining the grains' centroids, termed as *normal component*, and a component in the orthogonal direction, termed as *tangent component*. These relative displacement components are, in turn, decomposed into elastic and plastic parts. The elastic strain and dissipation energy functionals for a grain-grain interaction are then defined in terms of these components of the relative displacement (i.e. the reversible kinematic descriptors of the grain-grain interaction) [43, 42], the damage variables and the plastic multipliers (i.e. the irreversible kinematic descriptors of the grain-grain interaction). For each grain-grain interaction, damage is described by normal and tangent damage variables. Only plastic relative displacement accumulated in the normal direction will be here considered because, as shown in the sequel, for the assumptions that we have made here, no effects are entailed by accounting for plastic grain-grain relative displacement accumulated in the tangent direction. On the one hand, such a plastic relative displacement is not constrained to be non-decreasing in time. Indeed, it is not a plastic multiplier. On the other hand, it is defined as a difference of two non-decreasing plastic multipliers representing, respectively, the accumulated plastic relative displacement in tension and in compression. Numerical results obtained considering cyclic loading-unloading histories will be reported later on to elucidate the hysteretic features of the continuum emerging from such simple grain-grain interactions. The evolution of the load-free shape will be shown not only to assess the plastic behavior, but also to make tangible the point that, in the proposed approach, plastic strain is found to be intrinsically compatible with the existence of a placement function. It is indeed a matter of facts that in existing approaches this property is not always guaranteed. In such a case, a supplementary artificial compatibility condition or other *ad hoc* remedies must be conceived.

The elastic behavior of the damaged material is characterized by means of the total elastic strain energy, which is expressed in terms of the strain energies associated to each grain-grain interaction. As a result, relationships are obtained for standard first gradient (4th order stiffness tensor), second gradient (6th order stiffness tensor) and first-second-gradient interaction (5th order stiffness tensor) elastic moduli as functions of parameters describing the micro-mechano-morphology, as well as functions of damage variables. Owing to plastic effects, two more terms come out of the procedure, accounting for pre-stress (2nd order tensor) and pre-hyperstress (3rd order tensor). A hemi-variational approach [9, 32, 36, 34, 37, 38, 35] is utilized to derive the Karush-Kuhn-Tucker (KKT) type conditions leading to evolution equations for grain-grain damage and plastic kinematic variables, as well as to derive conditions, in

the form of Euler-Lagrange equations, for the evolution of grain-grain total relative displacement. The key advantage of making use of a postulation scheme based solely upon a variational statement is that evolution equations for damage and plastic variables are derived from first principles systematically, thus yielding robust criteria for loading-unloading-reloading conditions, without invoking supplementary thermodynamic principles that might be potentially incompatible with previous hypotheses. Furthermore, admissible boundary conditions are derived from the variational deduction procedure and are not postulated, again, in a possibly inconsistent way.

It is worth noting that, for a typical granular system, grain-pairs are oriented in various directions. Hence, under a given loading-sequence, they will experience different loading histories. Therefore, differently-oriented grain-grain interactions will experience different damage and plastic evolution. Additionally, for each grain-grain orientation, damage is defined for normal and tangential directions, and plasticity is characterized by two different plastic multipliers, i.e accumulation of normal plastic relative displacement in tension and compression. The overall macroscopic response will thus be very complex and strongly path-dependent.

The content of this paper is organized as follows. Section 2 discusses and elaborates Piola's ansatz, linking discrete and continuum descriptions. An objective measure of grain-grain relative displacement, as well as constitutive assumptions, are introduced within a finite deformation second-gradient framework. Section 3 deals with the definition of the elastic strain energy associated to each grain-grain interaction. Section 4 is devoted to the hemi-variational deduction procedure leading to Euler-Lagrange equilibrium equations, as well as to KKT conditions. Section 5 reports the results of numerical loading-unloading tests performed on a square plate deforming both homogeneously and non-homogeneously. Section 6 addresses some concluding remarks and future outlooks.

2 Discrete and continuum modeling of granular systems

2.1 Identification via Piola's ansatz

Within the discrete description, the reference configuration of the considered set of N grains is given by their positions $\{\boldsymbol{X}_1, \boldsymbol{X}_2, \ldots, \boldsymbol{X}_N\} \in \left(E^2\right)^N$, where E^2 is the Euclidean two-dimensional space. The position $\boldsymbol{x}_i \in E^2$, with $i = 1, \ldots, N$. in the present (or current) configuration, at time t, is obtained through the placement function $\boldsymbol{\chi}_i(t)$ as follows

$$\boldsymbol{x}_i = \boldsymbol{\chi}_i(t) = \boldsymbol{X}_i + u_i(t), \qquad i = 1, \ldots, N, \tag{1}$$

where $u_i(t)$ is the displacement function of the i-th grain. Within the continuum description, a continuous body $\mathcal{B}$, constituted by infinitely many particles, is considered in the reference configuration. A generic particle occupies the position $\boldsymbol{X}$ in the reference configuration, i.e. $\boldsymbol{X} \in \mathcal{B}$. Such a particle is placed, in the present configuration at time t, into the position x through the placement function

$$\boldsymbol{x} = \boldsymbol{\chi}(\boldsymbol{X}, t) = \boldsymbol{X} + u(\boldsymbol{X}, t), \tag{2}$$

where $u(\boldsymbol{X}, t)$ is the displacement function of the continuous body $\mathcal{B}$. In the continuum-discrete identification, the following relationship (Piola's Ansatz) will be assumed

$$\boldsymbol{\chi}(\boldsymbol{X}_i, t) = \boldsymbol{\chi}_i(t), \qquad i = 1, \ldots, N, \tag{3}$$

which means that the placements $\boldsymbol{\chi}_i(t)$ of the N grains correspond to the placement $\boldsymbol{\chi}(\boldsymbol{X}, t)$ of the continuous body $\mathcal{B}$ evaluated at those positions $\boldsymbol{X} = \boldsymbol{X}_i$, with $i = 1, ..., N$, where the grains are located in the reference configuration.

2.2 Relative grain-grain displacement and continuum deformation measures

Let us assume that the distance between two grain centroids at positions $\boldsymbol{X}_n$ and $\boldsymbol{X}_p$, respectively, is equal to L. Furthermore, let the unit vector $\hat{c}$ be defined as follows

$$\boldsymbol{X}_n - \boldsymbol{X}_p = \hat{c}L. \tag{4}$$

Therefore, the vectorial quantity $\hat{c}L$ in Eq. (4) is nothing but the arrow in the reference configuration that, once applied to the position $\boldsymbol{X}_n$, touches and points toward the position $\boldsymbol{X}_p$. In the current configuration, at time t, the

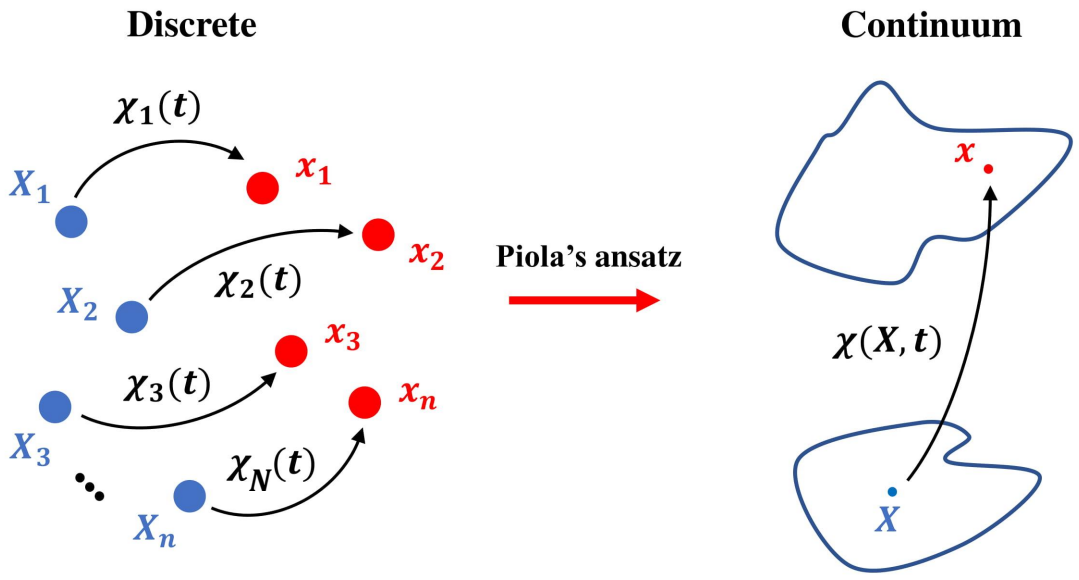

Figure 1: Graphical representation of Piola's Ansatz in Eq. (3). Discrete kinematic descriptors introduced in Eq. (1), on the left, and continuous kinematic descriptor introduced in Eq. (2), on the right.

positions occupied by the two grain centroids at positions $\boldsymbol{X}_n$ and $\boldsymbol{X}_p$ in the reference configuration are, respectively, $\boldsymbol{x}_n = \boldsymbol{\chi}(\boldsymbol{X}_n, t)$ and $\boldsymbol{x}_p = \boldsymbol{\chi}(\boldsymbol{X}_p, t)$. Analogously, the vector in Eq. (4) is transformed in the present configuration, at time t, into

$$\boldsymbol{x}_n - \boldsymbol{x}_p = \boldsymbol{\chi}(\boldsymbol{X}_n, t) - \boldsymbol{\chi}(\boldsymbol{X}_p, t). \tag{5}$$

Following [46], an objective relative displacement is defined as

$$u^{np} = F^T(\boldsymbol{x}_n - \boldsymbol{x}_p) - (\boldsymbol{X}_n - \boldsymbol{X}_p), \tag{6}$$

where $F = \nabla\boldsymbol{\chi}$ is the deformation gradient and a justification is given in the appendix 7.

Let us now assume that the two grains n and p are neighboring ones. Thus, they place similarly in the present configuration- The Taylor's series expansion of the function $\boldsymbol{\chi}(\boldsymbol{X}_n, t)$ centered at $\boldsymbol{X} = \boldsymbol{X}_p$ yields

$$\boldsymbol{x}_n = \boldsymbol{\chi}(\boldsymbol{X}_n, t) \cong \boldsymbol{x}_p + LF_p\hat{c} + \frac{L^2}{2}\left[\nabla_p F\hat{c}\right]\cdot\hat{c}, \tag{7}$$

where the following second and third order tensors evaluated at $\boldsymbol{X} = \boldsymbol{X}_p$ have been defined

$$F_p = (\nabla\boldsymbol{\chi})_{X=X_p}, \qquad \nabla_p F = \left[\nabla(\nabla\boldsymbol{\chi})\right]_{\boldsymbol{X}=\boldsymbol{X}_p}.$$

Let us also introduce the Green-Saint-Venant tensor G and its gradient, which are, respectively, a second and third order tensor

$$G = \frac{1}{2}\left(F^T F - I\right), \quad \nabla G = F^T\nabla F. \tag{8}$$

Equations (7) and (8), in index notation, where superscripts denote the position at which the corresponding quantity is evaluated, read as

$$x_i^n = x_i^p + F_{ij}^p\hat{c}_j L + \frac{L^2}{2}F_{ij,h}^p\hat{c}_j\hat{c}_h, \quad G_{ij}^p = \frac{1}{2}\left(F_{ai}^p F_{aj}^p - \delta_{ij}\right), \quad G_{ij,h}^p = F_{ai}^p F_{aj,h}^p. \tag{9}$$

Thus, making use of the index notation and taking into account Eqs. (4) and (9), the objective relative displacement in Eq. (6) can be re-written as

$$u_i^{np} = 2G_{ij}^p \hat{c}_j L + \frac{L^2}{2} G_{ij,h}^p \hat{c}_j \hat{c}_h. \tag{10}$$

We remark that, owing to Eq. (10), the objective relative displacement u^{np} for a given grain-grain orientation $\hat{c}$ is not additive inverse of that computed for the opposite grain-grain orientation, i.e. $-\hat{c}$, when the strain gradient is non-vanishing, i.e. $\nabla G \neq 0$, because it is not an odd function of $\hat{c}$. This means that the strain gradient breaks the symmetry with respect to the inversion of the grain-grain orientation. Such a feature enables strain-gradient-triggered chiral effects.

The half-projection of the objective relative displacement on the unit vector $\hat{c}$ is the so-called normal displacement u_η (a scalar quantity), while its projection on the unit vector orthogonal to $\hat{c}$ is the so-called tangent displacement vector

$$u_\eta = \frac{1}{2} u^{np} \cdot \hat{c}, \quad u_\tau = u^{np} - (u^{np} \cdot \hat{c})\, \hat{c}, \tag{11}$$

where a justification of the definitions (11) is given in the appendix 7. Insertion of (10) into (11) yields the normal displacement, its square and the squared tangent displacements, in terms of the strain G, the strain gradient ∇G, the grain-grain distance L and its orientation $\hat{c}$

$$u_\eta = L G_{ij} \hat{c}_i \hat{c}_j + \frac{L^2}{4} G_{ij,h} \hat{c}_i \hat{c}_j \hat{c}_h, \tag{12}$$

$$u_\eta^2 = L^2 \hat{c}_i \hat{c}_j \hat{c}_a \hat{c}_b G_{ij} G_{ab} + \frac{1}{2} L^3 \hat{c}_i \hat{c}_j \hat{c}_a \hat{c}_b \hat{c}_c G_{ij} G_{ab,c} + \frac{1}{16} L^4 \hat{c}_i \hat{c}_j \hat{c}_h \hat{c}_a \hat{c}_b \hat{c}_c G_{ij,h} G_{ab,c}, \tag{13}$$

$$u_\tau^2 = 4L^2 G_{ij} G_{ab} \left(\delta_{ia} \hat{c}_j \hat{c}_b - \hat{c}_i \hat{c}_j \hat{c}_a \hat{c}_b\right) + 2L^3 G_{ij} G_{ab,c} \left(\delta_{ia} \hat{c}_j \hat{c}_b \hat{c}_c - \hat{c}_i \hat{c}_j \hat{c}_a \hat{c}_b \hat{c}_c\right) \tag{14}$$

$$+ \frac{L^4}{4} G_{ij,h} G_{am,n} \left(\delta_{ia} \hat{c}_j \hat{c}_h \hat{c}_m \hat{c}_n - \hat{c}_i \hat{c}_j \hat{c}_h \hat{c}_a \hat{c}_b \hat{c}_c\right),$$

where the superscript p has been omitted to simplify the notation.

2.3 Elastic and plastic objective relative displacements

The elastic part u_η^{el} of the normal displacement u_η is assumed to be equal to the difference of the total normal displacement u_η and its plastic part u_η^{pl}

$$u_\eta^{el} = u_\eta - u_\eta^{pl} = L G_{ij} \hat{c}_i \hat{c}_j + \frac{L^2}{4} G_{ij,h} \hat{c}_i \hat{c}_j \hat{c}_h - u_\eta^{pl}. \tag{15}$$

Thus, its square is

$$\left(u_\eta^{el}\right)^2 = \left(u_\eta - u_\eta^{pl}\right)^2 = L^2 \hat{c}_i \hat{c}_j \hat{c}_a \hat{c}_b G_{ij} G_{ab} + \frac{1}{2} L^3 \hat{c}_i \hat{c}_j \hat{c}_a \hat{c}_b \hat{c}_c G_{ij} G_{ab,c} + \frac{L^4}{16} \hat{c}_i \hat{c}_j \hat{c}_h \hat{c}_a \hat{c}_b \hat{c}_c G_{ij,h} G_{ab,c}$$

$$+ \left(u_\eta^{pl}\right)^2 - 2L u_\eta^{pl} \hat{c}_i \hat{c}_j G_{ij} - \frac{1}{2} L^2 u_\eta^{pl} \hat{c}_i \hat{c}_j \hat{c}_h G_{ij,h}. \tag{16}$$

As remarked above, the tangent displacement u_τ is a vector. The only objective quantity that can be derived from u_τ and $\hat{c}$ is thus the square of u_τ in (14). Therefore, the plastic tangent displacement is defined only by its square $u_\tau^{pl,2}$, as well as its corresponding elastic part $u_\tau^{el,2}$, that yields,

$$u_\tau^{el,2} = u_\tau^2 - u_\tau^{pl,2}. \tag{17}$$

It is worth to anticipate here that, in Section 3, the plastic tangent relative displacement will be proved to give, for the assumptions that have been made, no contribution to the mechanical properties of the material.

2.4 Equivalent stiffnesses

Following the same notation employed in [46], the damaged tangent stiffness is denoted with $k_{\tau,D}$ and the damaged normal stiffness is denoted with $k_{\eta,D}$

$$k_{\eta,D} = k^t_{\eta,D}\Theta\left(u^{el}_\eta\right) + k^c_{\eta,D}\Theta\left(-u^{el}_\eta\right), \tag{18}$$

where $k^t_{\eta,D}$ is the stiffness in tension and $k^c_{\eta,D} \gg k^t_{\eta,D}$ is the stiffness in compression. Remark that, usually, for cementitious granular materials the stiffness in compression is much higher than the stiffness in tension. Here, tension and compression are discriminated through the sign of the elastic normal displacement u^{el}_η and, for this reason, we make use of the Heaviside function Θ. Damage is modeled with two variables, i.e. the normal damage D_η, and the tangent damage D_τ. The damage variables D_η and D_τ reduce linearly, respectively, the tension and compression normal damaged stiffness $k_{\eta,D}$ (18) and the tangent damaged stiffness $k_{\tau,D}$. In formulas, we have

$$k^t_{\eta,D} = k^t_\eta\left(1 - D_\eta\right), \qquad k^c_{\eta,D} = k^c_\eta\left(1 - D_\eta\right), \qquad k_{\tau,D} = k_\tau\left(1 - D_\tau\right), \tag{19}$$

which means that the tangent damaged stiffness $k_{\tau,D}$ and the normal damaged stiffness $k_{\eta,D}$ are defined, respectively, through the non-damaged tangent stiffness k_τ and the non-damaged normal stiffness k_η. For the latter case, in formulas, we have $k_{\eta,D} = k_\eta\left(1 - D_\eta\right)$, where the non-damaged normal stiffness k_η has been defined in terms of the non-damaged tension normal stiffness k^t_η and the non-damaged compression normal stiffness k^c_η as

$$k_\eta = k^t_\eta\Theta\left(u^{el}_\eta\right) + k^c_\eta\Theta\left(-u^{el}_\eta\right). \tag{20}$$

We hence obtain the following synthetic expression for the damaged normal stiffness

$$k_{\eta,D} = k_\eta\left(1 - D_\eta\right) = k^t_\eta\left(1 - D_\eta\right)\Theta\left(u^{el}_\eta\right) + k^c_\eta\left(1 - D_\eta\right)\Theta\left(-u^{el}_\eta\right). \tag{21}$$

3 Elastic strain energy function

The elastic energy density function per unit surface — for the continuum — is derived starting from the one elastic energy associated to a single grain-grain interaction, say the couple $n-p$ considered in Section 2.2, within the discrete description. We utilize to the scope a quadratic form of the recoverable elastic parts of the normal and tangent components of the objective total grain-grain relative displacement

$$U = \frac{1}{2}k_{\eta,D}\left(u^{el}_\eta\right)^2 + \frac{1}{2}k_{\tau,D}u^{el,2}_\tau, \tag{22}$$

where $\left(u^{el}_\eta\right)^2$ is the square of the scalar quantity u^{el}_η and $u^{el,2}_\tau$ is the squared module of the vector u^{el}_τ. The elastic energy function is a scalar quantity and, therefore, no coupling term between u^{el}_η and u^{el}_τ is admissible. It is worth to be noted that the damaged elastic stiffnesses in Eqs. $(19)_3$ and (21) can be defined as the coefficients of the quadratic form of the elastic energy function in Eq. (22).

In the discrete description, the total energy U^{tot} associated to the interaction of a given grain, whose centroid occupies the position X_p in the reference configuration, with neighboring grains is given by the summation of the energy in Eq. (22) for all the $N-1$ possible interactions

$$U^{tot} = \sum_{i=1}^{N-1}\left[\frac{1}{2}k_{\eta,D,i}\left(u^{el}_{\eta,i}\right)^2 + \frac{1}{2}k_{\tau,D,i}\left(u^{el,2}_{\tau,i}\right)\right], \tag{23}$$

where the subscript i refers to a generic couple $n-p$ of grains. In Eq. (23) it is therefore intended that $k_{\eta,D,i}$ and $k_{\tau,D,i}$ are the damaged stiffnesses, respectively normal and tangent, associated to the interaction of the i-th couple of grains, while $u^{el}_{\eta,i}$ and $u^{el,2}_{\tau,i}$ are the elastic relative displacements, respectively normal and squared tangent, of the i-th couple of grains.

Continualization of Eq. (23) is performed by using the following homogenization rule. Let a be a generic quantity defined within the discrete description, such that a_i refers to the grain-grain interaction, identified with the index i,

between a generic grain n and a generic grain p. Let $a(\theta)$ be the continuous distribution of the quantity a over the orientation θ of the grain-pair formed by grain n and its neighboring grains. We have that, when the number N of grains within the discrete system tends to infinite, the following limit holds

$$\sum_{i=1}^{N} [a_i] \qquad \longrightarrow \qquad \int_{\mathcal{S}^1} a(\theta), \tag{24}$$

where $\mathcal{S}^1 = [0, 2\pi]$ is the unit circle, namely the domain of the function $a(\theta)$, i.e. the set of all orientations. Remark that $a_i = a(\theta_i)$, where θ_i is the orientation of the grain-pair formed by grain n and grain p, namely the orientation of the unit vector $\hat{c}$. The application of the homogenization rule in Eq. (24) to the total energy U^{tot} in Eq. (23) gives

$$U = \int_{\mathcal{S}^1} \left[\frac{1}{2} k_\eta (1 - D_\eta) \left(u_\eta^{el}\right)^2 + \frac{1}{2} k_\tau (1 - D_\tau) \left(u_\tau^{el,2}\right) \right], \tag{25}$$

where $k_\eta = \widetilde{k}_\eta(\theta)$, $k_\tau = \widetilde{k}_\tau(\theta)$, $D_\eta = \widetilde{D}_\eta(\theta)$, and $D_\tau = \widetilde{D}_\tau(\theta)$ replace, respectively, $k_{\eta,i}$, $k_{\tau,i}$, $D_{\eta,i}$, and $D_{\tau,i}$. Remark that these quantities are all functions of the orientation $\theta \in [0, 2\pi]$ of the generic grain-pair formed by grain n and its neighboring grains, namely

$$k_{\eta,i} \to \widetilde{k}_\eta(\theta), \quad k_{\tau,i} \to \widetilde{k}_\tau(\theta), \quad D_{\eta,i} \to \widetilde{D}_\eta(\theta), \quad D_{\tau,i} \to \widetilde{D}_\tau(\theta).$$

From Eqs. (16) and (17), the continuum elastic strain energy density per unit surface in Eq. (25) reads as

$$\begin{aligned}
U = & \int_{\mathcal{S}^1} \frac{1}{2} k_\eta (1 - D_\eta) \left(L^2 \hat{c}_i \hat{c}_j \hat{c}_a \hat{c}_b G_{ij} G_{ab} + \frac{1}{2} L^3 \hat{c}_i \hat{c}_j \hat{c}_a \hat{c}_b \hat{c}_c G_{ij} G_{ab,c} \right) \\
& + \int_{\mathcal{S}^1} \frac{1}{2} k_\eta (1 - D_\eta) \left(\frac{1}{16} L^4 \hat{c}_i \hat{c}_j \hat{c}_h \hat{c}_a \hat{c}_b \hat{c}_c G_{ij,h} G_{ab,c} + \left(u_\eta^{pl}\right)^2 - 2 L u_\eta^{pl} \hat{c}_i \hat{c}_j G_{ij} - \frac{1}{2} L^2 u_\eta^{pl} \hat{c}_i \hat{c}_j \hat{c}_h G_{ij,h} \right) \\
& + \int_{\mathcal{S}^1} \frac{1}{2} k_\tau (1 - D_\tau) \left(4 L^2 G_{ij} G_{ab} \left(\delta_{ia} \hat{c}_j \hat{c}_b - \hat{c}_i \hat{c}_j \hat{c}_a \hat{c}_b \right) + 2 L^3 G_{ij} G_{ab,c} \left(\delta_{ia} \hat{c}_j \hat{c}_b \hat{c}_c - \hat{c}_i \hat{c}_j \hat{c}_a \hat{c}_b \hat{c}_c \right) \right) \\
& + \int_{\mathcal{S}^1} \frac{1}{2} k_\tau (1 - D_\tau) \left(\frac{1}{4} L^4 G_{ij,h} G_{am,n} \left(\delta_{ia} \hat{c}_j \hat{c}_h \hat{c}_m \hat{c}_n - \hat{c}_i \hat{c}_j \hat{c}_h \hat{c}_a \hat{c}_b \hat{c}_c \right) \right) - \int_{\mathcal{S}^1} \frac{1}{2} k_\tau (1 - D_\tau) u_\tau^{pl,2}.
\end{aligned} \tag{26}$$

The previous expression can be re-written in a more compact form as

$$U = \frac{1}{2} \mathbb{C}_{ijab} G_{ij} G_{ab} + \mathbb{M}_{ijabc} G_{ij} G_{ab,c} + \frac{1}{2} \mathbb{D}_{ijhabc} G_{ij,h} G_{ab,c} + \mathbb{P}_{ij} G_{ij} + \mathbb{Q}_{ijh} G_{ij,h} + \mathbb{P}^\tau, \tag{27}$$

where, accounting for the symmetrization induced by the symmetry of the strain tensor G, the elastic stiffnesses $\mathbb{C}$, $\mathbb{M}$, $\mathbb{D}$, $\mathbb{P}$, $\mathbb{Q}$ and $\mathbb{P}^\tau$, are identified as follows

$$\mathbb{C}_{ijab} = L^2 \int_{\mathcal{S}^1} k_\eta \left(1 - D_\eta\right) \hat{c}_i \hat{c}_j \hat{c}_a \hat{c}_b \tag{28}$$

$$+L^2 \int_{\mathcal{S}^1} k_\tau \left(1 - D_\tau\right) \left(\left(\delta_{ia}\hat{c}_j\hat{c}_b + \delta_{ib}\hat{c}_j\hat{c}_a + \delta_{ja}\hat{c}_i\hat{c}_b + \delta_{jb}\hat{c}_i\hat{c}_a\right) - 4\hat{c}_i\hat{c}_j\hat{c}_a\hat{c}_b\right)$$

$$\mathbb{M}_{ijabc} = \frac{1}{4}L^3 \int_{\mathcal{S}^1} k_\eta \left(1 - D_\eta\right) \hat{c}_i \hat{c}_j \hat{c}_a \hat{c}_b \hat{c}_c \tag{29}$$

$$\frac{1}{4}L^3 \int_{\mathcal{S}^1} k_\tau \left(1 - D_\tau\right) \left(\left(\delta_{ia}\hat{c}_j\hat{c}_b + \delta_{ib}\hat{c}_j\hat{c}_a + \delta_{ja}\hat{c}_i\hat{c}_b + \delta_{jb}\hat{c}_i\hat{c}_a\right)\hat{c}_c - 4\hat{c}_i\hat{c}_j\hat{c}_a\hat{c}_b\hat{c}_c\right)$$

$$\mathbb{D}_{ijhabc} = \frac{1}{16}L^4 \int_{\mathcal{S}^1} k_\eta \left(1 - D_\eta\right) \hat{c}_i \hat{c}_j \hat{c}_h \hat{c}_a \hat{c}_b \hat{c}_c \tag{30}$$

$$+\frac{1}{16}L^4 \int_{\mathcal{S}^1} k_\tau \left(1 - D_\tau\right) \left(\left(\delta_{ia}\hat{c}_j\hat{c}_b + \delta_{ib}\hat{c}_j\hat{c}_a + \delta_{ja}\hat{c}_i\hat{c}_b + \delta_{jb}\hat{c}_i\hat{c}_a\right)\hat{c}_h\hat{c}_c - 4\hat{c}_i\hat{c}_j\hat{c}_h\hat{c}_a\hat{c}_b\hat{c}_c\right)$$

$$\mathbb{P}_{ij} = -L \int_{\mathcal{S}^1} k_\eta \left(1 - D_\eta\right) u_\eta^{pl} \hat{c}_i \hat{c}_j \tag{31}$$

$$\mathbb{Q}_{ijh} = -\frac{1}{4}L^2 \int_{\mathcal{S}^1} k_\eta \left(1 - D_\eta\right) u_\eta^{pl} \hat{c}_i \hat{c}_j \hat{c}_h \tag{32}$$

$$\mathbb{P}^\tau = \int_{\mathcal{S}^1} \left[\frac{1}{2}k_\eta \left(1 - D_\eta\right) \left(u_\eta^{pl}\right)^2 - \frac{1}{2}k_\tau \left(1 - D_\tau\right) u_\tau^{pl,2}\right]. \tag{33}$$

From the previous results, we can conclude that, on one hand, the contribution of the squared tangent plastic relative displacement $u_\tau^{pl,2}$ does not have an influence on the mechanical behavior of the continuum, because it entails only the additive constant $\mathbb{P}^\tau$ in the continuum surface energy density 27. Remark that this deduction is not general and that, in particular, it comes from the assumption that has been done in Eq. (22) on the form of the grain-grain interaction. On the other hand, the contribution of the normal plastic relative displacement u_η^{pl} appears also in the stiffness tensors $\mathbb{P}$ and $\mathbb{Q}$, namely the coefficients of the linear terms (in G and ∇G, respectively) in the continuum surface energy density 27. These stiffness tensors define, respectively, the pre-stress and pre-hyper stress of the continuum. Hence, as shown in the sequel, they affect the load-free configuration.

Note that, in the hypothesis of small displacement gradients and small displacement second gradients, which means approximating up to second order the continuum strain energy density with respect to the displacement gradient H and its gradient, where H and its symmetric part E are defined as follows

$$H = \nabla u, \quad E = \frac{1}{2}\left(H + H^T\right), \tag{34}$$

we get

$$U = \frac{1}{2}\mathbb{C}_{ijab}E_{ij}E_{ab} + \mathbb{M}_{ijabc}E_{ij}E_{ab,c} + \frac{1}{2}\mathbb{D}_{ijhabc}E_{ij,h}E_{ab,c} + \mathbb{P}_{ij}E_{ij} \tag{35}$$

$$+\frac{1}{2}\mathbb{P}_{ij}H_{hi}H_{hj} + \mathbb{Q}_{ijh}E_{ij,h} + \frac{1}{2}\mathbb{Q}_{ijh}\left(H_{ki}H_{kj}\right)_{,h}.$$

Let us finally remark that, from the nontrivial expressions in Eqs. (29) and (32) for the stiffnesses $\mathbb{M}$ and $\mathbb{Q}$, respectively, which — inheriting the properties of the Taylor's series expansion in (7) — are not odd with respect to grain-pair's orientation, it is deduced that the occurrence of damage and plasticity, as well as of high strain gradients, induce the emergence of chiral effects. Note that, indeed, in the integrals (29) and (32), the unit vector $\hat{c}$ appears an odd number of times, while the domain is symmetric with respect to zero. Thus, while initially we have $\mathbb{M} = 0$ and $\mathbb{Q} = 0$, the evolution of damage variables D_η and D_τ, as well as of the plastic normal relative displacement u_η^{pl}, induces the emergence of chiral effects characterized by the conditions $\mathbb{M} \neq 0$ and $\mathbb{Q} \neq 0$.

4 Evolution of damage and plastic variables

4.1 Fundamental kinematic quantities

We evaluate the evolution of damage and plastic variables for each grain-grain interaction, namely for each orientation, via a deductive procedure based on a hemi-variational statement. To do this, we start by the definition of the following six (five scalar and one vectorial) fundamental kinematic quantities

$$u_\eta,\ u_\tau,\ D_\eta,\ D_\tau,\ \lambda_\eta^t,\ \lambda_\eta^c, \tag{36}$$

where u_η, u_τ, D_η and D_τ have been already defined in Subsections 2.2 and 2.4. The two plastic variables λ_η^t and λ_η^c are both associated to the normal relative displacement and are related, respectively, to tension and compression. Their difference gives the plastic normal displacement

$$u_\eta^{pl} = \lambda_\eta^t - \lambda_\eta^c. \tag{37}$$

As we have already pointed out, the tangent plastic variables do not play any role and, therefore, they will not be considered henceforth.

4.2 Dissipation, external and total energies

The dissipation energy W is the energy dissipated because of irreversible phenomena. An additive decomposition of the dissipation energy is assumed as follows

$$W = W_D + W_{pl}, \tag{38}$$

where W_D is the energy dissipated because of damage phenomena, while W_{pl} is the energy dissipated because of plasticity phenomena. The damage dissipation energy W_D is, see e.g. [46], in turn decomposed additively into normal, i.e. W_D^η, and tangent, i.e. W_D^τ, parts

$$W_D = W_D^\eta + W_D^\tau. \tag{39}$$

The normal contribution W_D^η to the damage dissipation energy is defined as follows

$$\begin{aligned} W_D^\eta = {} & \frac{1}{2} k_\eta^c \left(B_\eta^c\right)^2 \Theta\left(-u_\eta^{el}\right) \left[-D_\eta + \frac{2}{\pi}\tan\left(\frac{\pi}{2} D_\eta\right)\right] + \\ & \frac{1}{2} k_\eta^t \left(B_\eta^t\right)^2 \Theta\left(u_\eta^{el}\right) \left[2 + (D_\eta - 1)\left(2 - 2\log\left(1 - D_\eta\right) + \left(\log\left(1 - D_\eta\right)\right)^2\right)\right], \end{aligned} \tag{40}$$

where B_η^c and B_η^t are two characteristic lengths associated to normal damage dissipation in compression and in tension, respectively. We observe that usually, for cementitious materials, we have $B_\eta^t \ll B_\eta^c$. Indeed, a much smaller amount of elastic relative displacement is needed in tension to activate damage mechanisms. The tangent contribution W_D^τ to the damage dissipation energy is defined as follows

$$W_D^\tau = \frac{1}{2} k_\tau \left[\widetilde{B}_\tau\left(u_\eta^{el}\right)\right]^2 \left[2 + (D_\tau - 1)\left(2 - 2\log\left(1 - D_\tau\right) + \left(\log\left(1 - D_\tau\right)\right)^2\right)\right], \tag{41}$$

where $B_\tau = \widetilde{B}_\tau\left(u_\eta^{el}\right)$ is the characteristic length associated to tangent damage dissipation. Such a characteristic length is assumed to depend only on the elastic part of the normal relative grain-grain displacement, whereas in [29, 30] it is assumed to depend on the total normal displacement u_η. Additionally, differently from [29, 30] and for the sake of simplicity, the effect of the mean stress has been neglected. Following said references, the functional dependence $\widetilde{B}_\tau\left(u_\eta^{el}\right)$ has been chosen as follows

$$B_\tau = \widetilde{B}_\tau\left(u_\eta^{el}\right) = \begin{cases} B_{\tau 0} & \text{if } u_\eta^{el} \geq 0 \\ B_{\tau 0} - \alpha_2 u_\eta^{el} & \text{if } \frac{1-\alpha_1}{\alpha_2} B_{\tau 0} \leq u_\eta^{el} < 0 \\ \alpha_1 B_{\tau 0} & \text{if } u_\eta^{el} < B_{\tau 0}\frac{1-\alpha_1}{\alpha_2}, \end{cases} \tag{42}$$

where $B_{\tau 0}$ (B_{w0} in [29, 30]), α_1 and α_2 are further constitutive parameters needed to express the functional dependence $\widetilde{B}_\tau\left(u_\eta^{el}\right)$. Such a functional dependence couples the two addends W_D^η and W_D^τ of the decomposition (39). We observe that usually, for cementitious materials in elastic tension, the characteristic length B_τ associated to damage dissipation is much lower than the one in compression. Indeed, a smaller amount of elastic relative displacement is needed in extension to activate damage mechanisms. In formulas, referring to Eq. (42), this means either that $B_{\tau 0} << B_{\tau 0} - \alpha_2 u_\eta^{el}$ (which implies $\alpha_2 > 0$, as $u_\eta^{el} < 0$ in compression) or $B_{\tau 0} << \alpha_1 B_{\tau 0}$ (which implies $\alpha_1 \gg 1$).
The plastic dissipation energy function W_{pl} is assumed to depend linearly onto the plastic multipliers λ_η^t and λ_η^c

$$W_{pl} = \sigma_\eta^t \lambda_\eta^t + \sigma_\eta^c \lambda_\eta^c, \tag{43}$$

where the scalars σ_η^t and σ_η^c dictate the yielding conditions of the damage-elasto-plastic grain-grain interaction in tension and compression, respectively. Recently, Placidi [34] proved that, for such a dissipation energy functional, there is no change of the grain-grain interaction elastic range or, equivalently, the yielding conditions do not change when the system evolves.

In conclusion, because of Eqs. (39), (40), (41), and (43), the dissipation energy functional (38) reads as

$$\begin{aligned} &W = W_D + W_{pl} = W_D^\eta + W_D^\tau + W_{pl} = \\ &= \frac{1}{2} k_\eta^c \Theta\left(-u_\eta^{el}\right) B_c^2 \left[-D_\eta + \tan\left(D_\eta\right)\right] + \\ &+ \frac{1}{2} k_\eta^t \Theta\left(u_\eta^{el}\right) B_t^2 \left[2 + \left(D_\eta - 1\right)\left(2 - 2\log\left(1 - D_\eta\right) + \left(\log\left(1 - D_\eta\right)\right)^2\right)\right] \\ &+ \frac{1}{2} k_\tau B_\tau^2 \left[2 + \left(D_\tau - 1\right)\left(2 - 2\log\left(1 - D_\tau\right) + \left(\log\left(1 - D_\tau\right)\right)^2\right)\right] \\ &+ \sigma_\eta^t \lambda_\eta^t + \sigma_\eta^c \lambda_\eta^c \end{aligned} \tag{44}$$

Within the considered approach, the external world can exert forces expending power both on the scalar normal objective relative displacement u_η and on the vector tangent objective relative displacement u_τ, so that the external energy functional is

$$U^{ext} = F_\eta^{ext} u_\eta + F_\tau^{ext} \cdot u_\tau, \tag{45}$$

where F_η^{ext} and F_τ^{ext} are, respectively, the external normal and tangent forces. Since we are neglecting kinetic energy and considering quasi-static evolution, the energy functional $\mathcal{E}$ reads as

$$\mathcal{E} = \int_{T_0}^{T_M} \left[U + W - U^{ext}\right]. \tag{46}$$

Remark that it is a functional of the fundamental kinematical quantities (36), namely

$$\mathcal{E} = \mathcal{E}\left(u_\eta, u_\tau, D_\eta, D_\tau, \lambda_\eta^t, \lambda_\eta^c\right). \tag{47}$$

4.3 Formulation of the hemi-variational principle

The variational inequality principle can be here applied similarly to what has been done in [46], with the difference that, here, an extended set of kinematic descriptors must be considered. We introduce a monotonously increasing time sequence $T_i \in \{T_i\}_{i=0,\ldots,M}$ with $T_i \in \mathbb{R}$ and $M \in \mathbb{N}$. An initial datum on each of the fundamental kinematic quantities must be given for $i = 0$, i.e. for time T_0. A motion is defined as a family of displacements $\zeta = (u_\eta, u_\tau)$ defined for each time $t = T_0, T_1, \ldots, T_M$. The set AM_t is defined as the set of kinematically admissible displacements for a given time t — we require $(u_\eta, u_\tau) \in AM_t$ — and the set AV_t is defined as the corresponding space of kinematically admissible variations — i.e. $\upsilon = (\delta u_\eta, \delta u_\tau) \in AV_t$. Admissible variations β of the irreversible kinematic quantities $\left(D_\eta, D_\tau, \lambda_\eta^t, \lambda_\eta^c\right)$ must be positive, namely

$$\beta = \delta D_\eta, \delta D_\tau, \delta\lambda_\eta^t, \delta\lambda_\eta^c \in \mathbb{R}^+ \times \mathbb{R}^+ \times \mathbb{R}^+ \times \mathbb{R}^+. \tag{48}$$

The first variation $\delta\mathcal{E}$ of the energy functional (47) is defined as

$$\delta\mathcal{E} = \mathcal{E}\left(u_\eta + \delta u_\eta, u_\tau + \delta u_\tau, D_\eta + \delta D_\eta, D_\tau + \delta D_\tau, \lambda_\eta^t + \delta\lambda_\eta^t, \lambda_\eta^c + \delta\lambda_\eta^c\right) - \mathcal{E}\left(u_\eta, u_\tau, D_\eta, D_\tau, \lambda_\eta^t, \lambda_\eta^c\right). \tag{49}$$

The increment of the fundamental kinematic quantities (36) at $t = T_i$ is given by the difference between these quantities as evaluated at times $t = T_i$ and $t = T_{i-1}$, namely

$$\left(\Delta u_\eta, \Delta u_\tau, \Delta D_\eta, \Delta D_\tau, \Delta\lambda_\eta^t, \Delta\lambda_\eta^c\right)_{T_i} = \left(u_\eta, u_\tau, D_\eta, D_\tau, \lambda_\eta^t, \lambda_\eta^c\right)_{T_i} - \left(u_\eta, u_\tau, D_\eta, D_\tau, \lambda_\eta^t, \lambda_\eta^c\right)_{T_{i-1}}.$$

The same definition is utilised for the increment $\Delta\mathcal{E}$ of the energy functional

$$\Delta\mathcal{E} = \mathcal{E}\left(u_\eta + \Delta u_\eta, u_\tau + \Delta u_\tau, D_\eta + \Delta D_\eta, D_\tau + \Delta D_\tau, \lambda_\eta^t + \Delta\lambda_\eta^t, \lambda_\eta^c + \Delta\lambda_\eta^c\right) - \mathcal{E}\left(u_\eta, u_\tau, D_\eta, D_\tau, \lambda_\eta^t, \lambda_\eta^c\right). \tag{50}$$

Finally, the hemi-variational principle is formulated as follows

$$\Delta\mathcal{E} \leq \delta\mathcal{E} \qquad \forall\upsilon = (\delta u_\eta, \delta u_\tau) \in AV_t, \qquad \forall\beta = \left(\delta D_\eta, \delta D_\tau, \delta\lambda_\eta^t, \delta\lambda_\eta^c\right) \in \mathbb{R}^+ \times \mathbb{R}^+ \times \mathbb{R}^+ \times \mathbb{R}^+. \tag{51}$$

4.4 Derivation of the Euler-Lagrange equations

The variational inequality (51) must be exploited following the same procedure described in [46], which will thus be omitted here. The results of such a procedure are the following two Euler-Lagrange equations

$$\left\{-k_\eta\left(1 - D_\eta\right)\left(u_\eta - \lambda_\eta^t + \lambda_\eta^c\right) - k_\tau B_\tau \frac{\partial\widetilde{B}_\tau}{\partial u_\eta^{el}} \int_0^{D_\tau} \left[\log\left(1 - x\right)\right]^2 dx + F_\eta^{ext}\right\}(\delta u_\eta) = 0$$

$$\left\{-k_\tau\left(1 - D_\tau\right)u_\tau + F_\tau^{ext}\right\}(\delta u_\tau) = 0$$

together with the two KKT conditions for damage variables (already derived in [46])

$$\left[\left(u_\eta - \lambda_\eta^t + \lambda_\eta^c\right)^2 - \Theta\left(u_\eta^{el}\right) B_t^2 \left(\log\left(1 - D_\eta\right)\right)^2 - \Theta\left(-u_\eta^{el}\right) B_c^2 \left[\tan\left(D_\eta\right)\right]^2\right]\Delta D_\eta = 0, \tag{52}$$

$$\left[\left(u_\tau\right)^2 - \left[B_\tau\right]^2 \left(\log\left(1 - D_\tau\right)\right)^2\right]\Delta D_\tau = 0, \tag{53}$$

and two additional KKT conditions for the plastic multipliers, namely

$$\left\{k_\eta\left(1 - D_\eta\right)\left(u_\eta - \lambda_\eta^t + \lambda_\eta^c\right) - \sigma_\eta^t + k_\tau B_\tau \frac{\partial\widetilde{B}_\tau}{\partial u_\eta^{el}} \left[\int_0^{D_\tau} \left[\log\left(1 - x\right)\right]^2 dx\right]\right\}\Delta\lambda_\eta^t = 0, \tag{54}$$

$$\left\{k_\eta\left(1 - D_\eta\right)\left(u_\eta - \lambda_\eta^t + \lambda_\eta^c\right) + \sigma_\eta^c + k_\tau B_\tau \frac{\partial\widetilde{B}_\tau}{\partial u_\eta^{el}} \left[\int_0^{D_\tau} \left[\log\left(1 - x\right)\right]^2 dx\right]\right\}\Delta\lambda_\eta^c = 0, \tag{55}$$

where the following formula has been taken into account

$$\int_0^{D_\tau} \left[\log\left(1 - x\right)\right]^2 dx = 2 + \left(D_\tau - 1\right)\left(2 - 2\log\left(1 - D_\tau\right) + \left(\log\left(1 - D_\tau\right)\right)^2\right).$$

The four KKT conditions (52), (53), (54) and (55) for irreversible descriptors can be arranged in a more compact form as

$$\left\{D_\eta - \tilde{D}_\eta(u_\eta, \lambda_\eta^t, \lambda_\eta^c)\right\}\Delta D_\eta = 0 \tag{56}$$

$$\left\{D_\tau - \tilde{D}_\tau(u_\tau)\right\}\Delta D_\tau = 0 \tag{57}$$

$$\left\{\lambda_\eta^t - \tilde{\lambda}_\eta^t(u_\eta, \lambda_\eta^c, D_\eta, D_\tau)\right\}\Delta\lambda_\eta^t = 0 \tag{58}$$

$$\left\{\lambda_\eta^c - \tilde{\lambda}_\eta^c(u_\eta, \lambda_\eta^t, D_\eta, D_\tau)\right\}\Delta\lambda_\eta^c = 0, \tag{59}$$

where the auxiliary threshold functions $\tilde{D}_\eta(u_\eta, \lambda_\eta^t, \lambda_\eta^c)$, $\tilde{D}_\tau(u_\tau)$, $\tilde{\lambda}_\eta^t(u_\eta, \lambda_\eta^c, D_\eta, D_\tau)$ and $\tilde{\lambda}_\eta^c(u_\eta, \lambda_\eta^t, D_\eta, D_\tau)$ have been defined as follows

$$\tilde{D}_\eta(u_\eta, \lambda_\eta^t, \lambda_\eta^c) = \begin{cases} 1 - \exp\left(-\frac{u_\eta - \lambda_\eta^t + \lambda_\eta^c}{B_\eta^t}\right), & u_\eta^{el} = u_\eta - \lambda_\eta^t + \lambda_\eta^c > 0, \\ \frac{2}{\pi}\arctan\left(-\frac{u_\eta - \lambda_\eta^t + \lambda_\eta^c}{B_\eta^c}\right), & u_\eta^{el} = u_\eta - \lambda_\eta^t + \lambda_\eta^c < 0, \end{cases} \tag{60}$$

$$\tilde{D}_\tau(u_\tau) = 1 - \exp\left(-\frac{|u_\tau|}{B_\tau}\right), \tag{61}$$

$$\tilde{\lambda}_\eta^t(u_\eta, \lambda_\eta^c, D_\eta, D_\tau) = \lambda_\eta^c - \frac{\sigma_\eta^t}{k_\eta(1 - D_\eta)} + u_\eta + \frac{k_\tau B_\tau}{k_\eta(1 - D_\eta)} \frac{\partial \widetilde{B}_\tau}{\partial u_\eta^{el}} \left[\int_0^{D_\tau} [\log(1 - x)]^2 \, dx\right], \tag{62}$$

$$\tilde{\lambda}_\eta^c(u_\eta, \lambda_\eta^t, D_\eta, D_\tau) = \lambda_\eta^t - \frac{\sigma_\eta^c}{k_\eta(1 - D_\eta)} - u_\eta - \frac{k_\tau B_\tau}{k_\eta(1 - D_\eta)} \frac{\partial \widetilde{B}_\tau}{\partial u_\eta^{el}} \left[\int_0^{D_\tau} [\log(1 - x)]^2 \, dx\right]. \tag{63}$$

5 Results

In this section, we intend to illustrate the properties of the model by numerical results presented for selected test cases. Two square specimens in 2D, with side $S = 10$ cm (Fig. 2), are subjected to cyclic tension-compression loading, as sketched in Fig. 3. The quantity $\bar{u}$ in Fig. 3 is null at the initial time and then ranges within the interval $[\bar{u}_{min}, \bar{u}_{max}]$. The first specimen, without any flaw, has been chosen to assess the performances of the solution scheme in the case of a homogeneous deformation, while the second, with a circular flaw (hole), has been chosen to address non-homogeneous deformations under the same set of kinematic boundary conditions used for the first specimen.

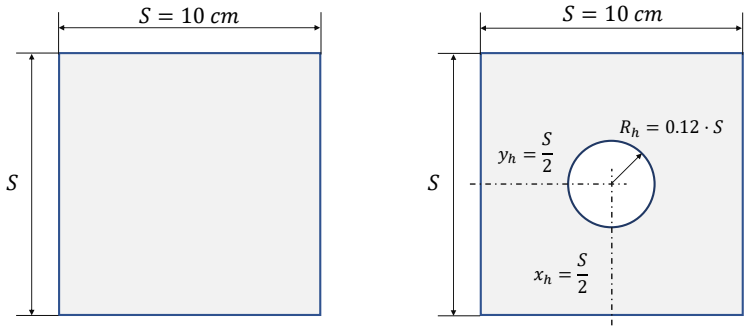

Figure 2: Schematics of analyzed domains, without (left-hand side) and with (right-hand side) the hole.

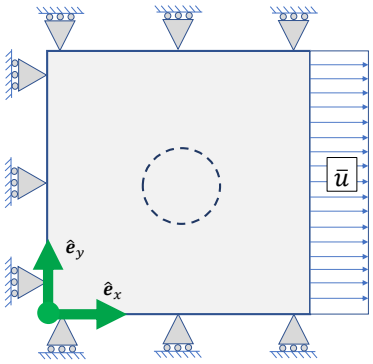

Figure 3: Schematics of the considered boundary condition: cyclic, extension (i.e. $\bar{u} > 0$) and compression (i.e. $\bar{u} < 0$) tests.

5.1 Implementation of the numerical algorithm

The test cases were investigated numerically by means of the commercial software Matlab and COMSOL Multiphysics. An iterative procedure was developed. It is schematized in the flowchart in Fig. 4.

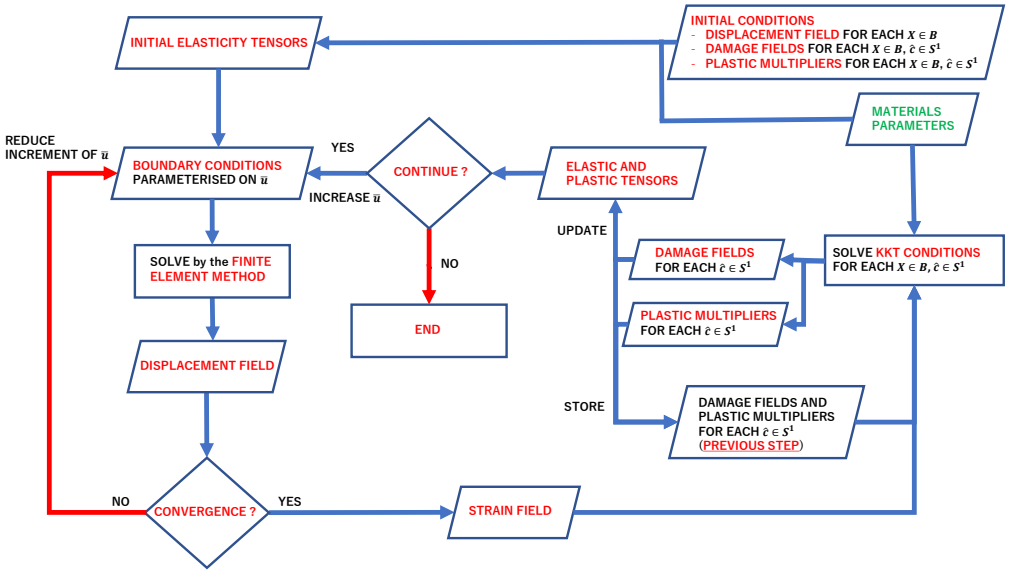

Figure 4: Flowchart of the numerical iterative procedure used to solve the mathematical formulation.

The steps of the procedure can be explained as follows:

1. We assume null initial conditions on the displacement field for all the points of the body

$$u\left(\boldsymbol{X}, t = T_0\right) = 0, \quad \forall \boldsymbol{X} \in \mathcal{B}$$

and null initial conditions for damage and plastic irreversible descriptors; not only for all the points of the body, but also for every orientation

$$\begin{cases} D_\eta = \breve{D}_\eta\left(\hat{c}, \boldsymbol{X}, t = T_0\right) = 0, & D_\tau = \breve{D}_\tau\left(\hat{c}, \boldsymbol{X}, t = T_0\right) = 0 \\ \lambda_\eta^t = \breve{\lambda}_\eta^t\left(\hat{c}, \boldsymbol{X}, t = T_0\right) = 0, & \lambda_\eta^c = \breve{\lambda}_\eta^c\left(\hat{c}, \boldsymbol{X}, t = T_0\right) = 0 \end{cases}, \qquad \forall \hat{c} \in \mathcal{S}^1 \quad \forall \boldsymbol{X} \in \mathcal{B}$$

The stiffnesses k_η^c, k_η^t and k_τ are assumed to be initially isotropic

$$k_\eta^c = \tilde{k}_\eta^c\left(\hat{c}, \boldsymbol{X}, t = T_0\right) = \frac{\bar{k}_\eta^c}{2\pi}, \quad k_\eta^t = \tilde{k}_\eta^t\left(\hat{c}, \boldsymbol{X}, t = T_0\right) = \frac{\bar{k}_\eta^t}{2\pi}, \quad k_\tau = \tilde{k}_\tau\left(\hat{c}, \boldsymbol{X}, t = T_0\right) = \frac{\bar{k}_\tau}{2\pi}, \qquad \forall \hat{c} \in \mathcal{S}^1 \quad \forall \boldsymbol{X} \in \mathcal{B},$$

where $\bar{k}_\eta^c$, $\bar{k}_\eta^t$ and $\bar{k}_\tau$ are the averaged initial stiffnesses. It is worth to observe that the effective (i.e. damaged) stiffnesses $k_{\eta,D}^c, k_{\eta,D}^t, k_{\tau,D}$ may change during the evolution of the system due to the non-trivial evolution of damage descriptors, that are induced by the state of deformation, thus leading to non-isotropic distribution of effective stiffness. Material parameters of the model are: the averaged initial stiffness $\bar{k}_\eta^c$, $\bar{k}_\eta^t$ and $\bar{k}_\tau$, the inter-granular interaction distance L, the damage characteristic lengths B_η^c, B_η^t and $B_{\tau 0}$ along with the non-dimensional characteristics α_1 and α_2, and the plastic yielding parameters σ_η^t and σ_η^c. Numerical values for these parameters, employed to obtain the subsequent simulation results, are reported in Tabs. 1-2.

2. The elasticity tensors $(\mathbb{C}_{ijab}, \mathbb{M}_{ijabc}, \mathbb{D}_{ijhabc})$, as well as the plasticity tensors $(\mathbb{P}_{ij}, \mathbb{Q}_{ijh})$ and $\mathbb{P}^\tau$, are calculated according to Eqs. (28-33). All these quantities, together with boundary conditions, are then given as input to a finite element subroutine consisting on a COMSOL Multiphysics run. The weak form of the equilibrium problem defined by the elastic energy per unit surface in Eq. (27) is solved by means of the *weak form* package. In order to ensure C^1 continuity across element's boundaries, Quintic Argyris polynomials are used as shape functions. A Delaunay-tessellated triangular mesh is employed;

3. The increment of the displacement field with respect to the previous step is node-wise compared with a tolerance. When such a tolerance is not respected, then the displacement parameter $\bar{u}$ is reduced to re-initialize the finite element subroutine;

4. When the increment of the displacement field with respect to the previous step compares positively with the above-mentioned chosen tolerance, then the displacement field is computed;

5. The strain and the strain gradient fields $[G]_j$ and $[\nabla G]_j$ are calculated at time $t = T_j$ and then used, by means of Eqs. (11), to compute normal $[u_\eta]_j$ and tangent $[u_\tau]_j$ displacements, for every position X and for every orientation $\hat{c}$. Such displacements are then given as input to the KKT conditions in Eqs. (56-59), taking into account the definitions (60-63). The damage $[D_\eta]_j$ and $[D_\tau]_j$ and plastic $\left[\lambda_\eta^t\right]_j$ and $\left[\lambda_\eta^c\right]_j$ descriptors at time $t = T_j$ are recovered as an output of KKT conditions as follows. We proceed by calculating firstly the damage descriptors by using the plastic multipliers $\left[\lambda_\eta^t\right]_{j-1}$ and $\left[\lambda_\eta^c\right]_{j-1}$ at the previous time step $t = T_{j-1}$ and normal $[u_\eta]_j$ and tangent $[u_\tau]_j$ displacements at the current step $t = T_j$

$$[D_\eta]_j = \max\left\{\tilde{D}_\eta\left([u_\eta]_j, \left[\lambda_\eta^t\right]_{j-1}, \left[\lambda_\eta^c\right]_{j-1}\right), [D_\eta]_{j-1}\right\}, \quad [D_\tau]_j = \max\left\{\tilde{D}_\tau\left([u_\tau]_j\right), [D_\tau]_{j-1}\right\}. \tag{64}$$

Subsequently, each plastic descriptor is computed using the other plastic descriptor at the previous time step $t = T_{j-1}$ and normal $[u_\eta]_j$ and tangent $[u_\tau]_j$ displacements and damage $[D_\eta]_j$ and $[D_\tau]_j$ at the current step $t = T_j$,

$$\left[\lambda_\eta^t\right]_j = \max\left\{\tilde{\lambda}_\eta^t\left([u_\eta]_j, \left[\lambda_\eta^c\right]_{j-1}, [D_\eta]_j, [D_\tau]_j\right), \left[\lambda_\eta^t\right]_{j-1}\right\}, \quad \left[\lambda_\eta^c\right]_j = \max\left\{\tilde{\lambda}_\eta^c\left([u_\eta]_j, \left[\lambda_\eta^t\right]_{j-1}, [D_\eta]_j, [D_\tau]_j\right), \left[\lambda_\eta^c\right]_{j-1}\right\} \tag{65}$$

Clearly, the order chosen to compute the above quantities is arbitrary and may be changed without causing, for small loading steps, relevant differences in the solution. Remark that the present computational scheme is explicit. In future works we intend to develop implicit schemes.

6. The load parameter $\bar{u}$ is increased or decreased depending on the phase (loading or unloading) of the numerical experiment.

The instructions above (from point 2) are repeated for the index j ranging from 1 to N_{it} until a termination criterion is not verified, i.e. the maximum number of cycles is reached. It is worth to mention that, aimed at smoothing the constitutive assumption in Eq. (20) we replace the Heaviside function $\Theta(x)$ by the following smooth one

$$\frac{1}{2} + \frac{1}{\pi}\arctan\left(\frac{x}{\alpha}\right), \tag{66}$$

so that the non-damaged normal stiffness is replaced by a smooth function of the elastic normal displacement

$$k_\eta = \frac{1}{2}\left(k_\eta^t + k_\eta^c\right) + \frac{1}{\pi}\left(k_\eta^t - k_\eta^c\right)\arctan\left(\frac{u_\eta^{el}}{\alpha}\right), \tag{67}$$

which, in turn, gives the damaged normal stiffness as a smooth function of the elastic normal displacement

$$k_{\eta,D} = \frac{1}{2}\left(k_\eta^t + k_\eta^c\right)(1-D_\eta) + \frac{1}{\pi}\left(k_\eta^t - k_\eta^c\right)\arctan\left(\frac{u_\eta^{el}}{\alpha}\right)(1-D_\eta). \tag{68}$$

The quantity α can be tuned to modulate the regularization. Large values of α enhance the convergence of the algorithm. A value for α is considered, see Tabs. 1-2, as to give a sufficiently smooth and non-stiff problem while not being detrimental to the congruence of Eqs. (20, 67) and Eqs. (21, 68), so that the physical meaning of α can be overlooked.

5.2 Homogeneous deformations

5.2.1 Preliminaries to the homogeneous case

It can be easily seen that, when the flawless (i.e. no hole) specimen is considered, then boundary conditions in Fig. 3 imply homogeneous deformations. Thus, strain gradient terms in the deformation energy are not activated, i.e. $\nabla G = 0$. The reason is that we have

$$u_1 = \frac{\bar{u}}{S}X_1,\ u_2 = 0, \quad \Rightarrow \quad F = \begin{pmatrix} 1+\frac{\bar{u}}{S} & 0 \\ 0 & 0 \end{pmatrix}, \quad \Rightarrow \quad G = \begin{pmatrix} \frac{1}{2}\left(\frac{\bar{u}}{S}\right)^2 + \frac{\bar{u}}{S} & 0 \\ 0 & 0 \end{pmatrix}, \quad \Rightarrow \quad \nabla G = 0, \tag{69}$$

and, from (12) and (14), normal and squared tangent displacement are

$$u_\eta = L\left[\frac{1}{2}\left(\frac{\bar{u}}{S}\right)^2 + \frac{\bar{u}}{S}\right](c_1)^2 = L\left[\frac{1}{2}\left(\frac{\bar{u}}{S}\right)^2 + \frac{\bar{u}}{S}\right]\cos^2\theta, \tag{70}$$

$$u_\tau^2 = 4L^2\left[\frac{1}{2}\left(\frac{\bar{u}}{S}\right)^2 + \frac{\bar{u}}{S}\right]^2\left((c_1)^2 - (c_1)^4\right) = \left(L\frac{\bar{u}}{S}\right)^2\left[1 + \left(\frac{\bar{u}}{S}\right) + \frac{1}{4}\left(\frac{\bar{u}}{S}\right)^2\right]\sin^2 2\theta, \tag{71}$$

where the angle θ characterizes the orientation of the unit vector $\hat{c}$ according to the following polar representation in an orthonormal frame of reference $(O, \hat{e}_1, \hat{e}_2)$

$$\hat{c} = c_1\hat{e}_1 + c_2\hat{e}_2 = \cos\theta\hat{e}_1 + \sin\theta\hat{e}_2. \tag{72}$$

First of all, we observe an elastic non-linear contribution in the strain tensor G, because it is not equal to the symmetric part of the displacement gradient, namely the tensor E defined in (34), but it is the non-linear Green-Saint-Venant strain tensor defined in (8), see also [?]. Besides, it is worth to be noted that, in the present uni-axial case (69), normal displacement (70) is maximum for horizontal grain-pair orientations ($\theta = i\pi$, with $i \in \mathbb{N}$) and minimum for vertical grain-pair orientations ($\theta = (1+2i)\,\pi/2$, with $i \in \mathbb{N}$) and the tangent displacement u_τ (71) is zero only for horizontal and vertical ($\theta = i\pi/2$, with $i \in \mathbb{N}$) grain-pair orientations, being maximum for oblique orientations ($\theta = (1+2i)\,\pi/4$, with $i \in \mathbb{N}$). Finally, according to the stiffness matrix evolution (28-33), we observe that homogeneous and initially isotropic sample becomes anisotropic due to damage and plastic evolution.

5.2.2 Plastic condition in tension, i.e. $\bar{u} \geq 0$

From (70), in the case of tension, the normal displacement u_η is positive for every grain-pair orientation $\hat{c}$. Thus, we have not only that the plastic compression multiplier is null, i.e. $\lambda_\eta^c = 0$, but also that the tangent damage characteristic length does not depend on the elastic normal displacement u_η^{el}, i.e.

$$\frac{\partial B_\tau}{\partial u_\eta^{el}} = 0.$$

Thus, the KKT conditions for the plastic tension multiplier λ_η^t and those for the damage descriptors, for the loading condition ($\Delta\lambda_\eta^t \geq 0$, $\Delta D_\eta \geq 0$ and $\Delta D_\tau \geq 0$) are

$$k_\eta \left(1 - D_\eta\right)\left(u_\eta - \lambda_\eta^t\right) - \sigma_\eta^t = 0, \quad D_\eta = 1 - \exp\left(-\frac{u_\eta - \lambda_\eta^t}{B_\eta^t}\right), \quad D_\tau = 1 - \exp\left(-\frac{|u_\tau|}{B_\tau}\right),$$

thus giving

$$\exp\left(X\right) = XA, \quad X > 0, \tag{73}$$

where the elastic normal displacement and the variables X and A are defined as

$$u_\eta^{el} = u_\eta - \lambda_\eta^t + \lambda_\eta^c = u_\eta - \lambda_\eta^t, \qquad X = \frac{u_\eta^{el}}{B_\eta^t}, \qquad A = \frac{k_\eta B_\eta^t}{\sigma_\eta^t}.$$

As a consequence, activation of plastic tension multiplier can be achieved only if Eq. (73) has roots, namely when the following condition is met

$$A = \frac{k_\eta B_\eta^t}{\sigma_\eta^t} > e, \tag{74}$$

where $e = \exp(1)$ is Euler's (or Napier's) number. This fact has been investigated in Fig. 5, where the homogeneous case is calculated with different values of A. The employed constitutive parameters are reported in Tab. 1 and results are shown in terms of force/displacement diagrams.

L[m]	$k_\eta^c[J/m^4]$	$k_\eta^t[J/m^4]$	$k_\tau[J/m^4]$	B_η^c[m]	$B_{\tau 0}$[m]	α_1[1]	α_2[1]	$\sigma_\eta^t[J/m^3]$	$\sigma_\eta^c[J/m^3]$	α[1]
0.01	$14 \cdot 10^{14}$	$14 \cdot 10^{13}$	$3 \cdot 10^{13}$	$1.5 \cdot 10^{-7}$	$5 \cdot 10^{-8}$	10	14	$4 \cdot 10^6$	$4 \cdot 10^7$	$0.5 \cdot 10^{-9}$

Table 1: Parameters' values employed for homogeneous tension tests and cyclic loading tests. Employed values of the normal characteristic damage length B_η^t in homogeneous tension tests, used to control the parameter A in Eq. (74), are reported in the corresponding figures. For cyclic loading tests, some of the parameters have different values from those reported in this table. For these test, the correct values are reported in Tab. 2.

It can be observed that for $B_\eta^t = 3.5 \cdot 10^{-8}$ and $B_\eta^t = 0.75 \cdot 10^{-7}$, i.e. when $A < e$, force/displacement diagrams show no plasticity at all, because the condition in Eq. (74) is not fulfilled. In such a case, the plastic multiplier λ_η^t remains equal to zero. By increasing B_η^t, we are able to change such a qualitative behavior. When $B_\eta^t = 0.8 \cdot 10^7$, we have $A = 2.8 > e$ and the condition in Eq. (74) is satisfied. In such a case, we have null reaction force for non-zero displacement. Increasing the value of the damage tension characteristic length, i.e. with $B_\eta^t = 3.5 \cdot 10^{-7}$, accumulation of plastic residual deformation is even more evident. It is worth to be noted also that the change of the slope of the force/displacement curve in the unloading part of the curve in Fig. 5 is governed by the change of normal stiffness from k_η^t to k_η^c when we pass from elastic tension ($u_\eta^{el} > 0$) to elastic compression ($u_\eta^{el} < 0$). This behavior it is expected for the plastic case, where the plastic deformation may imply that the tension case ($u_\eta^{el} > 0$) does not always imply the sign of the elastic normal displacement.

5.2.3 Cyclic loading with initial tension and with initial compression conditions

In this subsection, we investigate the plastic response under cyclic loading with initial tension condition and with initial compression condition. The first case is analyzed in Fig. 6, where the number of cycle N_{cycle} is $N_{cycle} = 1$ but a

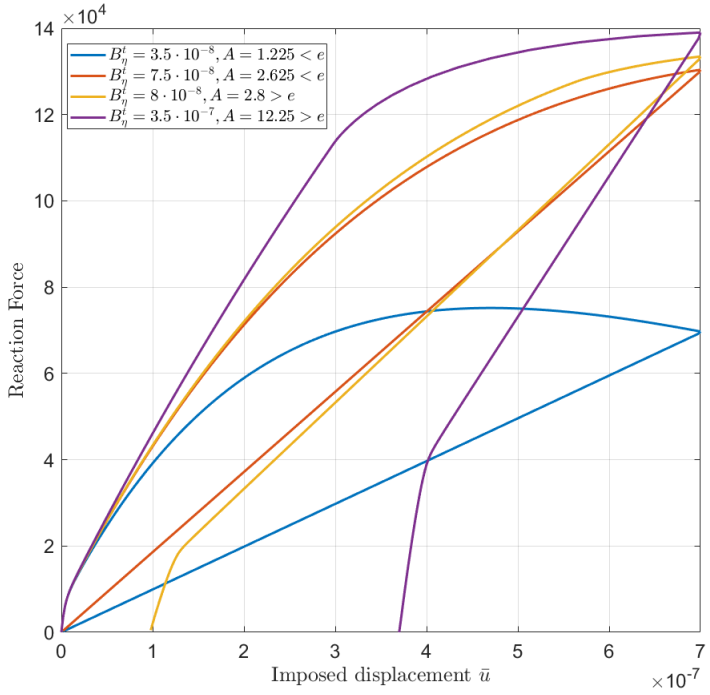

Figure 5: Force vs displacement diagrams for homogeneous tension test obtained for different tension normal characteristic damage lengths B_η^t. By changing $A = \frac{k_\eta B_\eta^t}{\sigma_\eta^t}$, we observe different material responses. Yellow and purple curves correspond to the case when the condition $A > e$ is satisfied. Red and blue curves, for which the condition $A > e$ is not fulfilled, end at the origin, namely zero reaction force corresponds to null prescribed displacement.

convergence analysis is done with respect to the time-step, and the second case in Fig. 7, where the number N_{cycle} of cycles is $N_{cycle} = 10$. In this second case, the first cycle starts with compression, decreasing the imposed displacement $\bar{u}$ from 0 to $\bar{u}_{min} < 0$. When the minimum value $\bar{u} = \bar{u}_{min}$ of the imposed displacement is hold, we increase $\bar{u}$ from $\bar{u}_{min} < 0$ to $\bar{u}_{max} > 0$. After that we finish the cycle decreasing the imposed displacement $\bar{u}$ from $\bar{u}_{max} > 0$ down to zero value $\bar{u} = 0$. Thus, the cycle is repeated a number N_{cycle} of times. In Fig. 7 force/displacement diagram for the case of $N_{cycle} = 10$ is presented. In order to make plasticity more evident we chose the highest value for the tension damage characteristic length B_η^t that was investigated in Fig. 5, and, in order to emphasize the damage growth, we reduce the tangent damage characteristic length $B_{\tau 0}$ according to the Tab. 2. In the tension parts of the curve that is shown in Fig. 7 we reach maximum plastic deformation already at the end of the first cycle and it does not change anymore in subsequent cycles. However, in the compression parts of the curve the situation is different. In fact, we have that up to the 5^{th} cycle, the reaction force is less than that of the previous cycle. This difference between tension and compression parts of the curve is due to the fact, that $\partial B_\tau / \partial u_\eta^{el} \neq 0$ in compression activating the last term in Eqs. (62, 63). We finally remark that, after the 5^{th} cycle, the maximum reaction force in compression remains the same till the end of the simulation and the reason is that plasticity has completely inhibited damage.

Figs. 8 and 9 show polar plots of the irreversible descriptors. In this homogeneous case, on the one hand they are uniform over the domain, but on the other hand they are a function of the grain-pair orientation $\hat{c}$ (or, because

B^t_η[m]	$B_{\tau 0}$[m]		N_{cycle}		N_θ	$\bar{u}_{min}$[m]	$\bar{u}_{max}$[m]	α[1]
	uniform	non-uniform	uniform	non-uniform				
$3.5 \cdot 10^{-7}$	$1 \cdot 10^{-7}$	$1 \cdot 10^{-6}$	10	2	120	$-1.2 \cdot 10^{-6}$	$4 \cdot 10^{-7}$	$1 \cdot 10^{-9}$

Table 2: Values of parameters used only for the cyclic loading tests. The quantity N_θ is the number of elements employed to discretize the orientation range $[0, 2\pi]$.

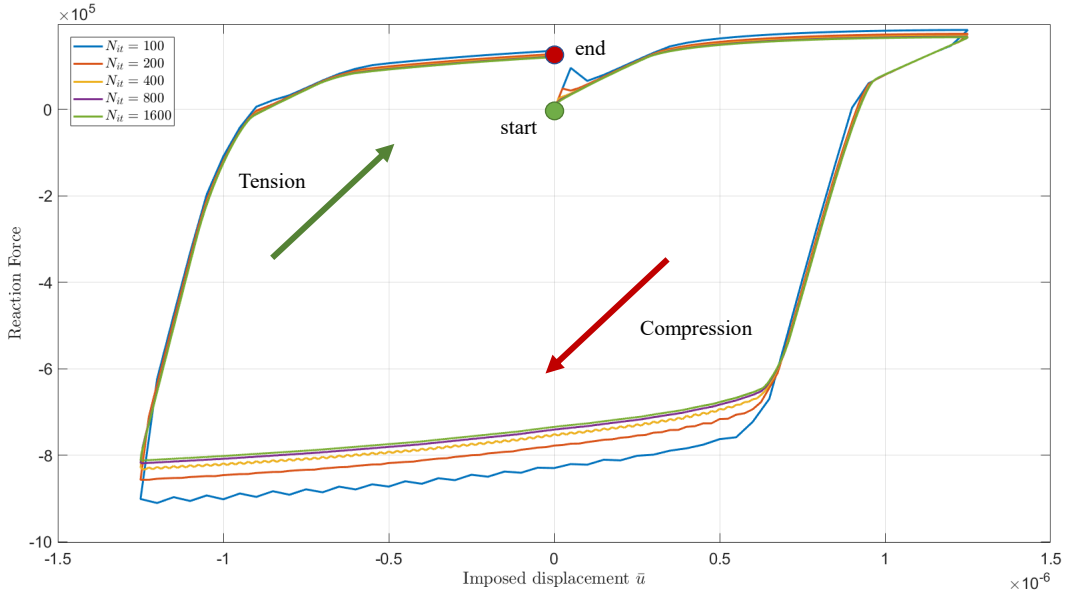

Figure 6: Force vs displacement diagram for homogeneous cyclic loading test with $N_{cycle} = 1$ and initial tension for different numbers N_{it} of iterations.

of (72), of the angle θ) and evolve with time. The dependence with respect to the angle θ is represented by the polar plot and the evolution with time is shown by the black arrows. The horizontal grain-pair orientation ($\theta = 0$ or $\theta = \pi$) corresponds to the direction of the applied load, which gives the fastest normal damage (left-hand side of Fig. 8) and plastic multipliers (Fig. 9) growth rate. Tangent damage (that is shown on the right-hand side of Fig. 8) evolves with (61). Thus, its evolution is affected both by the tangent displacement in the form of (71) and by the normal displacement via the definition of the shear damage characteristic length B_τ in Eq. (42). It is worth to be noted from polar plots of plastic multipliers, that are presented in Fig. 9, we estimate the number of cycles simply by following how curve density is changing with increasing $\bar{u}$. Finally, in the present homogeneous case, strain gradient is null, $\nabla G = 0$, that means from eqns. (12) and (11), a symmetry of normal and tangent displacement with respect to the grain-pair orientation inversion $\hat{c} \to -\hat{c}$, that imply the non-chiral behavior of the homogeneous case. The same symmetry holds for damage and plastic descriptors.

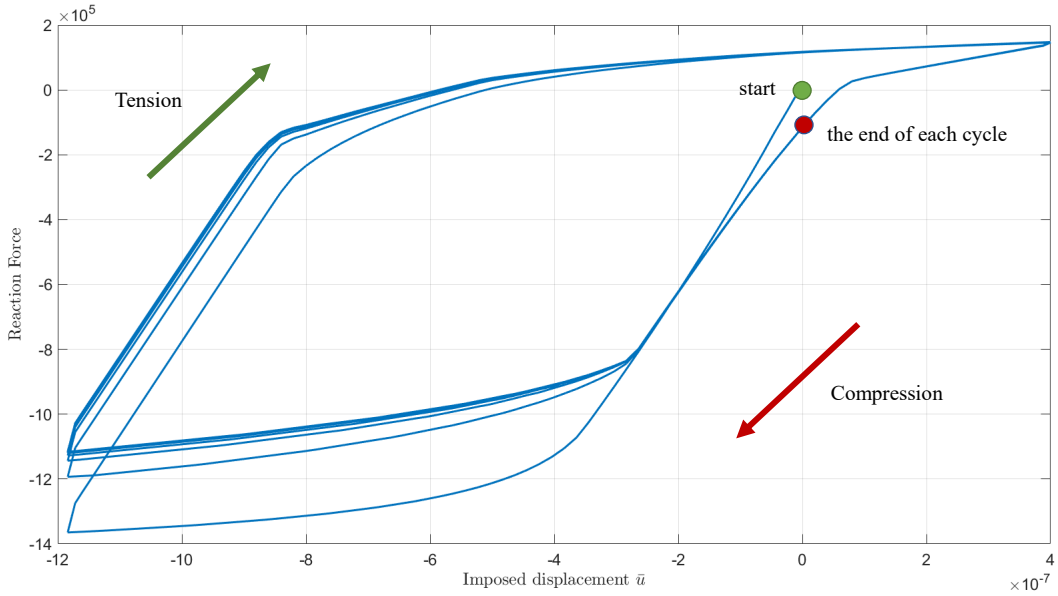

Figure 7: Force vs displacement diagram for homogeneous cyclic loading test with $N_{cycle} = 10$ and initial compression.

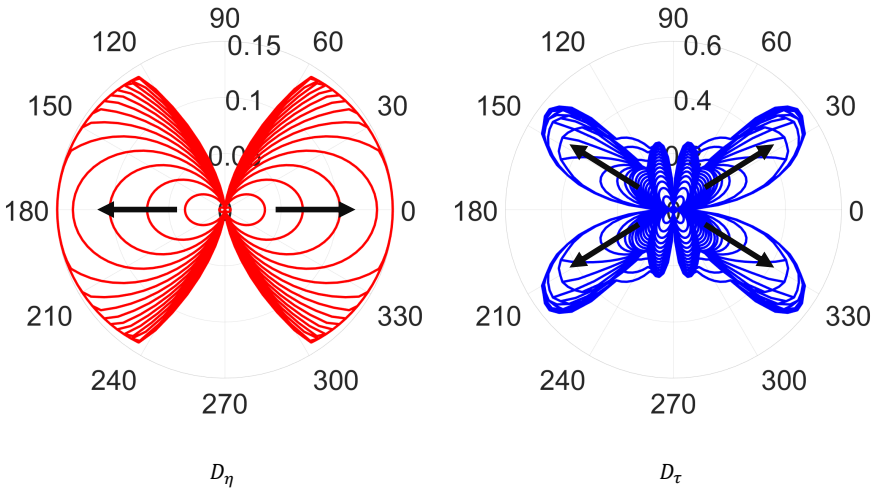

Figure 8: Homogeneous cyclic test with $N_{cycle} = 10$. Polar plots of normal D_η (left) and tangent D_τ (right) damage. Black arrows indicate directions of increasing loading time-step.

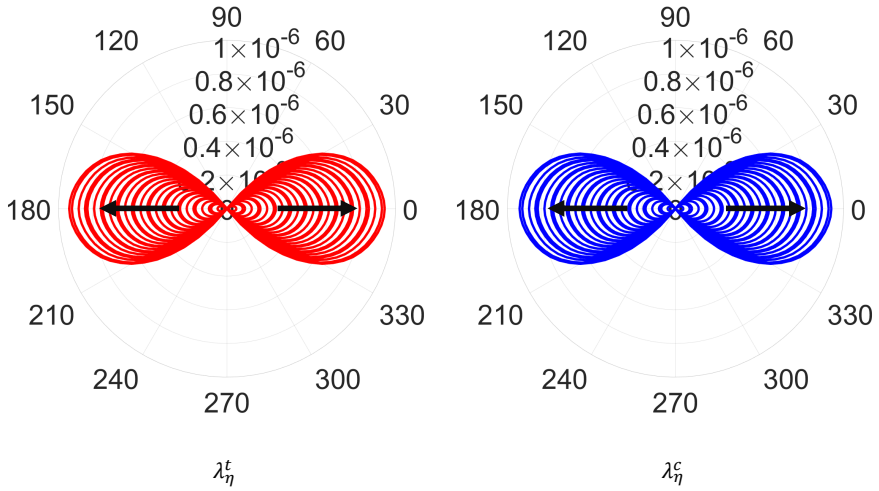

Figure 9: Homogeneous cyclic test with $N_{cycle} = 10$. Polar plots of plastic multipliers in tension λ_η^t (left) and in compression λ_η^c (right). Black arrows indicate directions of increasing loading time-step.

At the top of Fig. 10 we show the plastic relative displacement

$$\bar{u}_\eta^{pl}(t) = \frac{1}{2\pi}\int_{\mathcal{S}^1} \left(\lambda_\eta^t - \lambda_\eta^c\right) \tag{75}$$

averaged over all grain-pair orientations and as a function of time. At the bottom of the same Fig. 10 we show the plastic dissipation energy W_{pl} defined in (43). We observe that eventhough the plastic relative displacement is reversible in time, the dissipation energy, as expected, is a non-decreasing time-function.

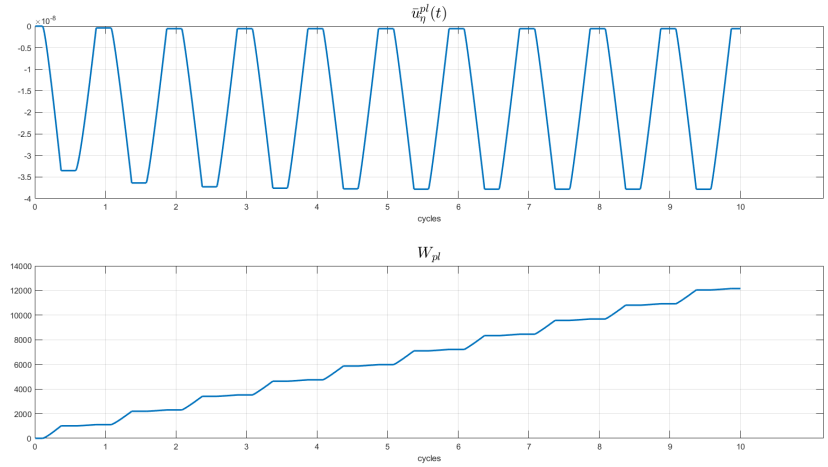

Figure 10: Homogeneous cyclic test with $N_{cycle} = 10$. Evolution of the averaged plastic displacement $\bar{u}_\eta^{pl}(t)$ (on the top) and of plastic dissipation energy W_{pl} (on the bottom) with the loading time t.

5.3 Non-homogeneous deformations under cyclic loading

We now proceed considering a non-uniform sample with a flaw under cyclic loading. Due to numerical costs we limit ourselves to a low number of cycles, i.e. $N_{cycle} = 2$.

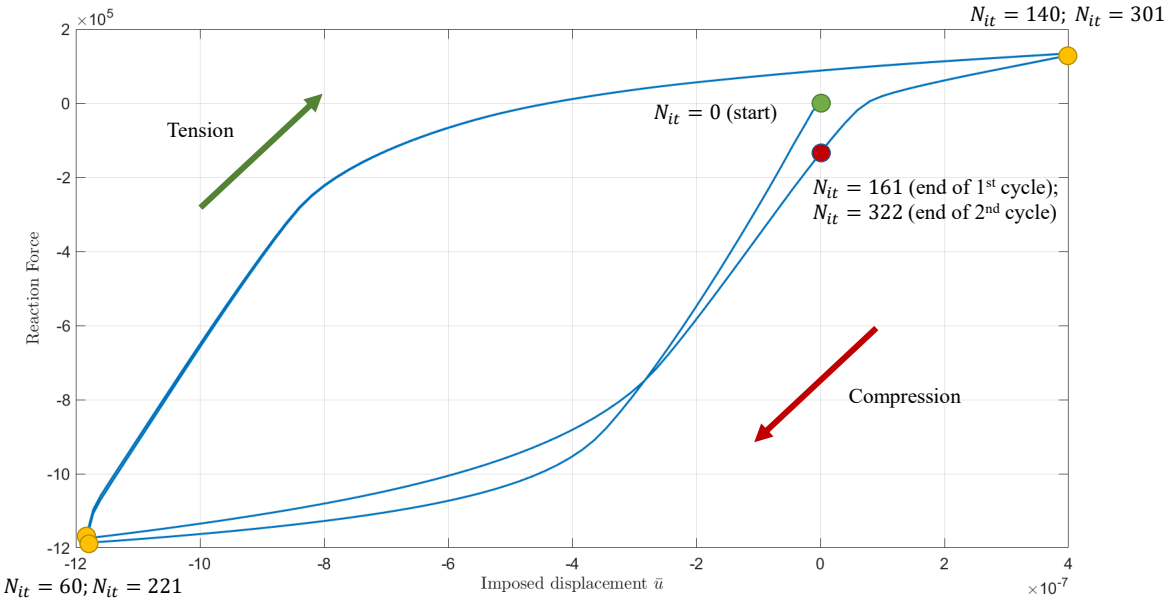

Figure 11: Force vs displacement diagram for non-homogeneous cyclic loading test with $N_{cycle} = 2$.

Figs. 12-13-14-15 show the polar plots of damage and plastic descriptors at different points of the specimen (at the external boundary in Figs. 12-14 and in the neighborhood of the flaw in Figs. 13-15) for the non-homogeneous cyclic test.

The heterogeneity of this case is shown by the fact that these polar plots are different in different points. Besides, strain-gradient ∇G is different from zero and becomes more and more relevant during the test especially for those points in the neighborhood of the flaw. It is therefore there that strain gradient effects is more evident. First of all the chiral symmetry $\hat{c} \to -\hat{c}$ does not hold for normal and tangent displacement in the neighboring of the hole and therefore also for damage and plastic descriptors, that yields the chiral behavior of the non-homogeneous case, that is evident for the internal points of Figs. 13 and 15.

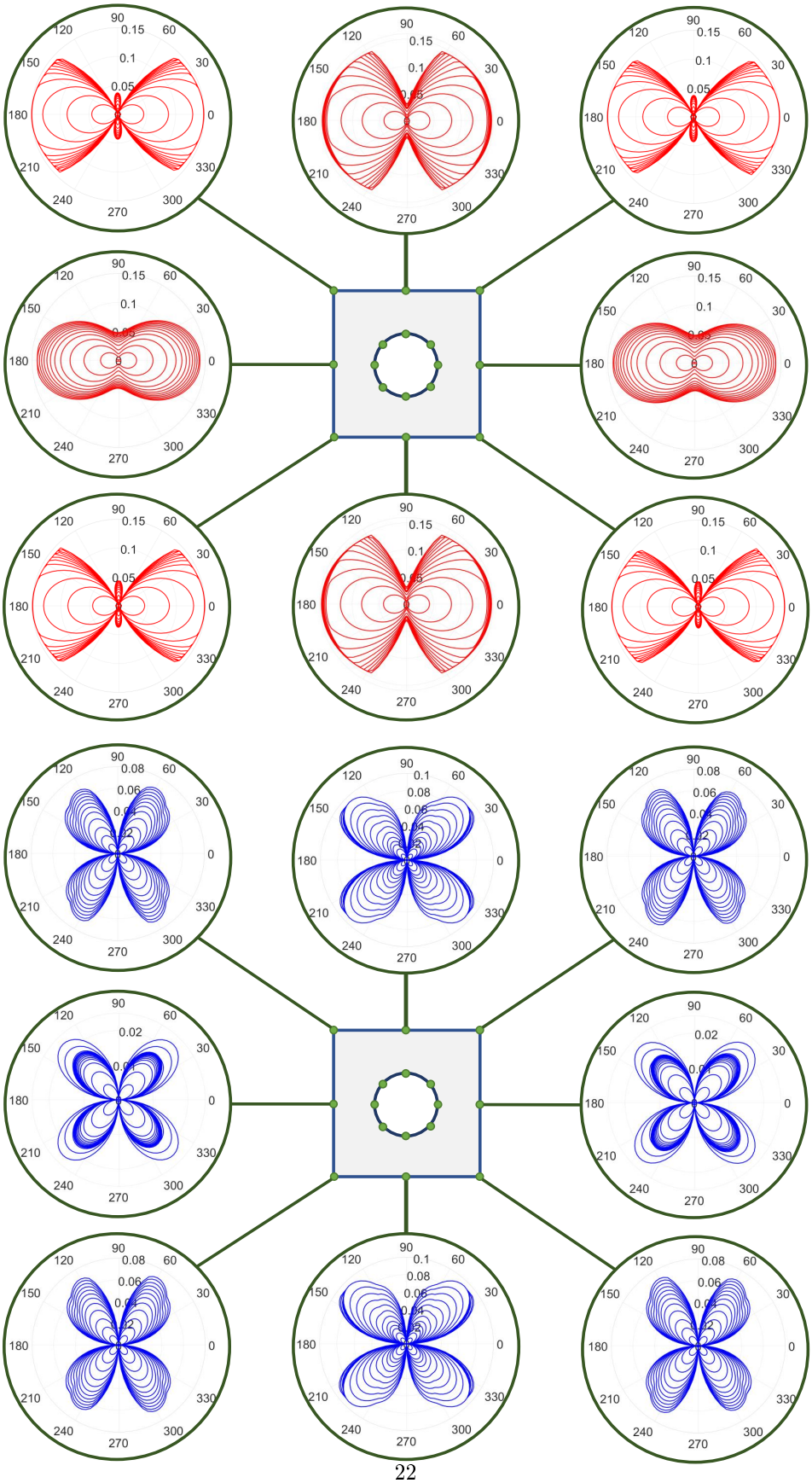

Figure 12: Normal D_η (top) and tangent D_τ (bottom) damage polar plot for external points in the non-homogeneous case.

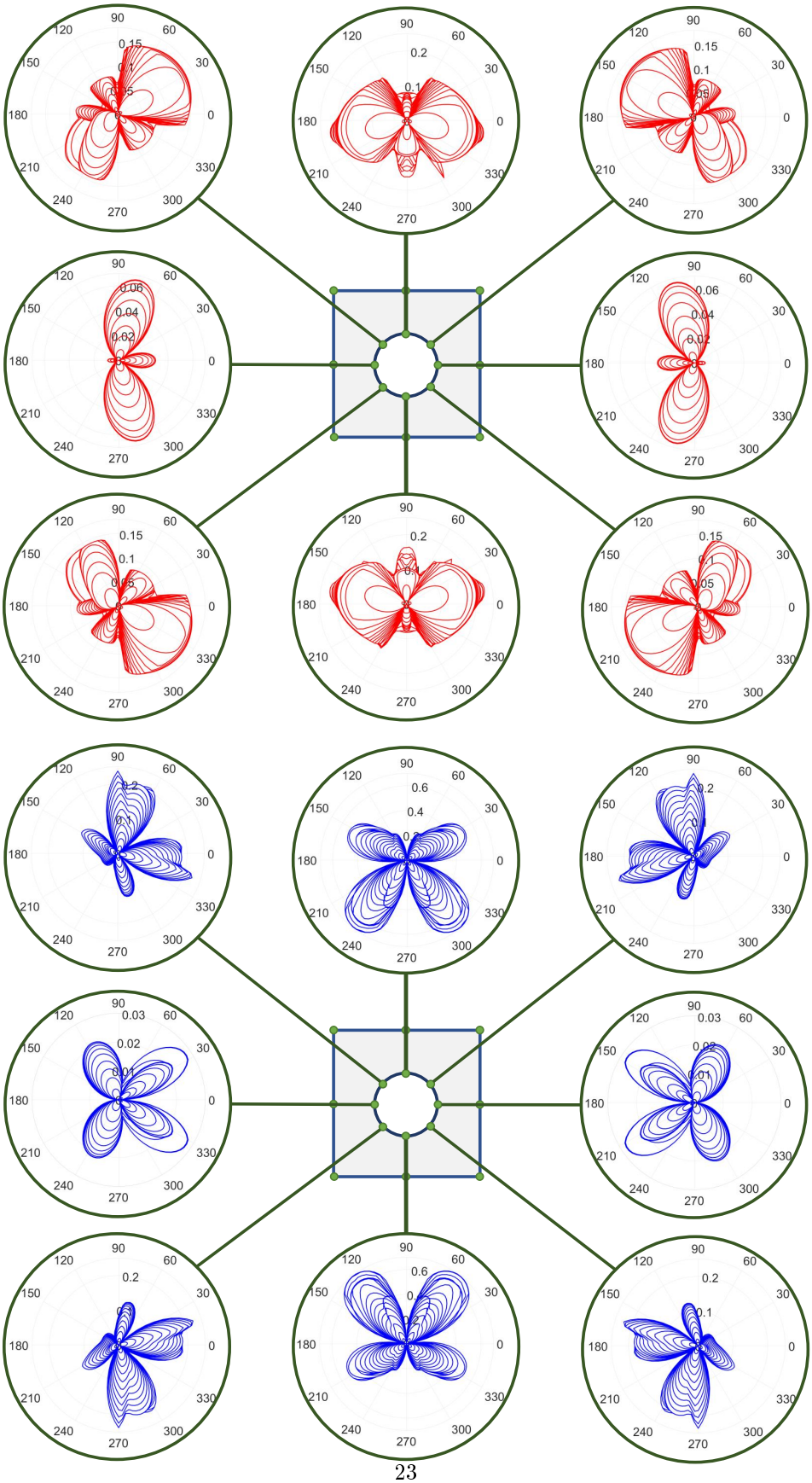

Figure 13: Normal D_η (top) and tangent D_τ (bottom) damage polar plots for internal points in the non-homogeneous case.

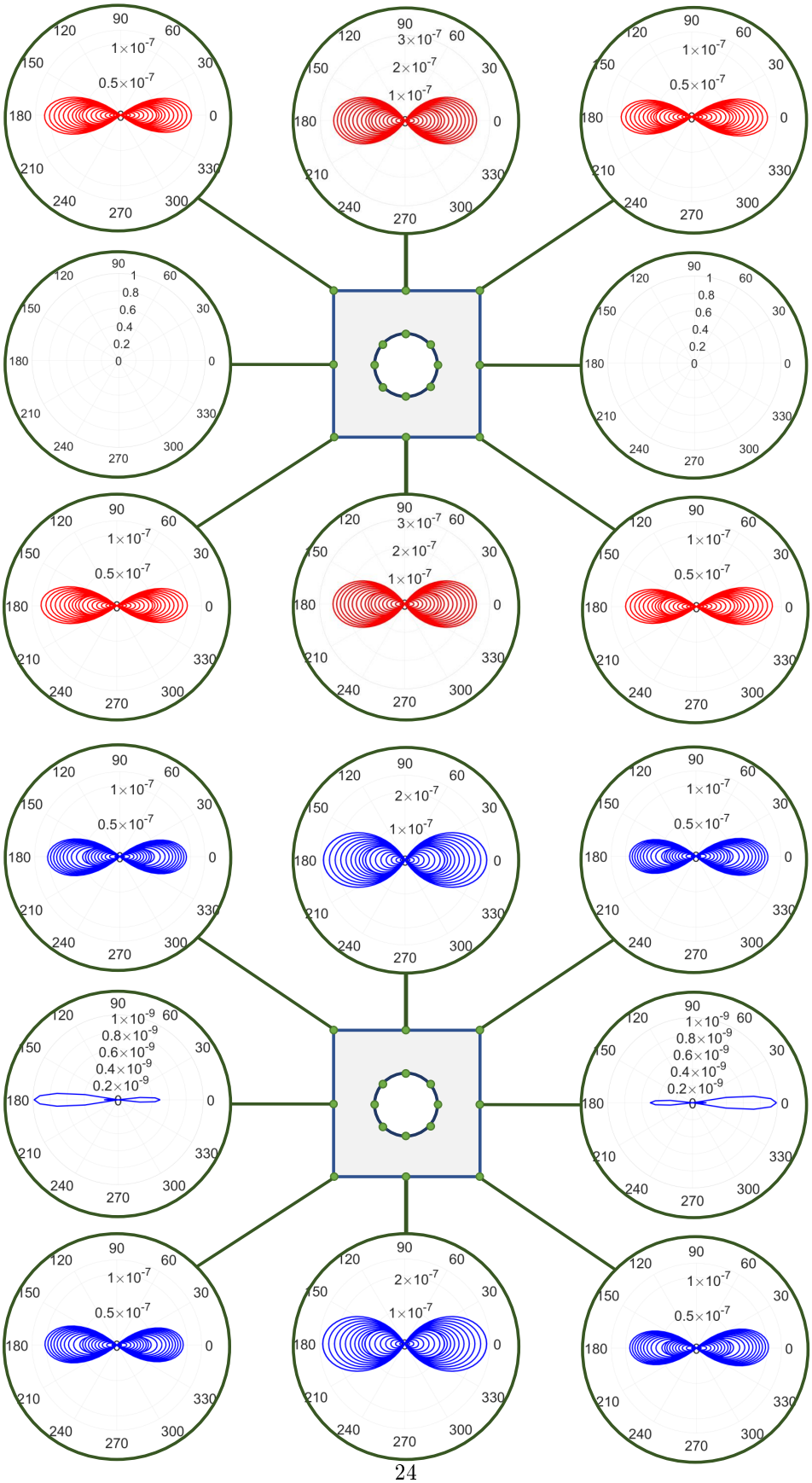

Figure 14: Tension λ_η^t (top) and compression λ_η^c (bottom) plastic multipliers polar plots for external points in the non-homogeneous case.

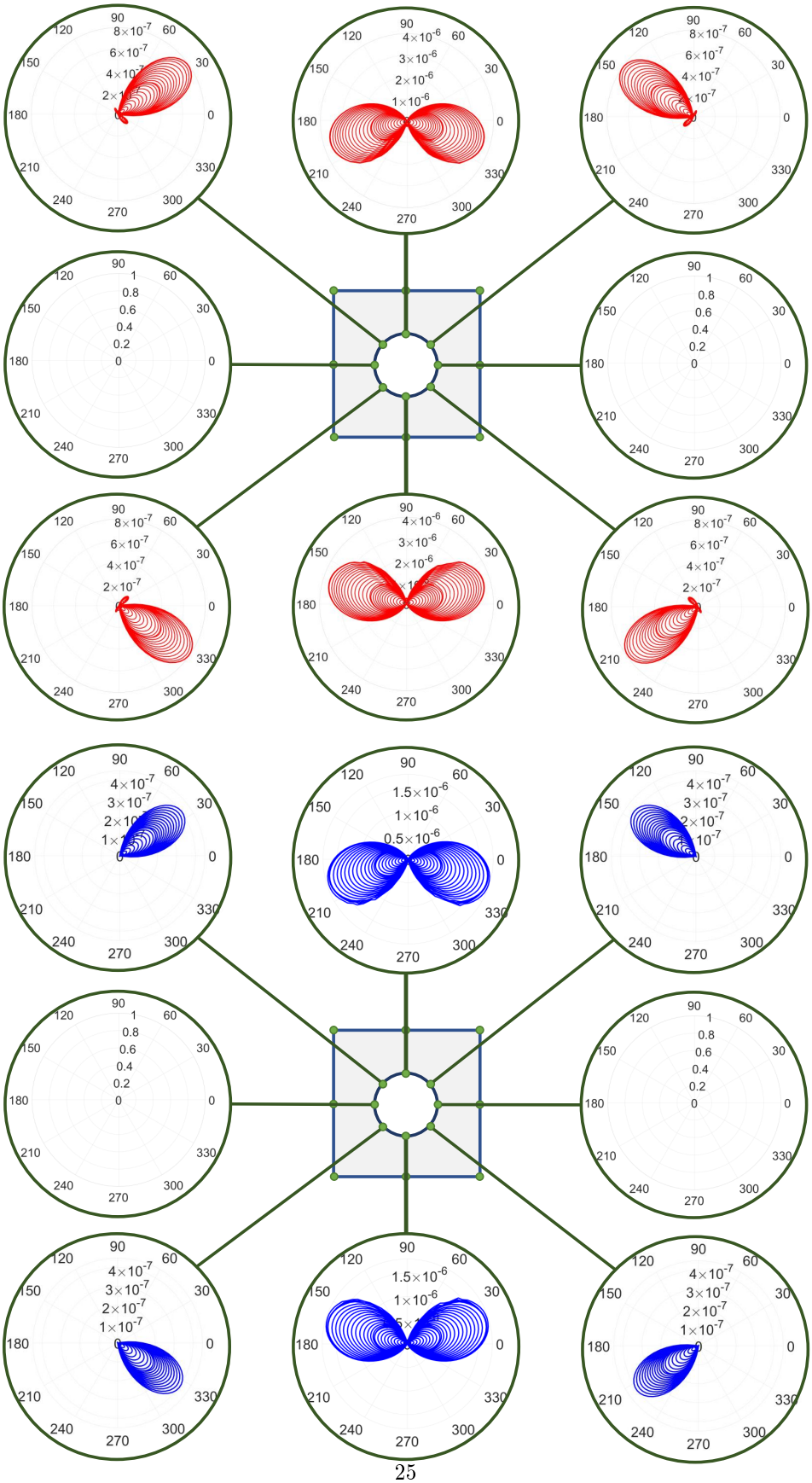

Figure 15: Tension λ_η^t (top) and compression λ_η^c (bottom) plastic multipliers polar plots for internal points in the non-homogeneous case.

Fig. 16 shows the contour plots of the average plastic displacement $\bar{u}^{pl}$ defined in (75) for different time-loading steps. It is clear that plasticity is evident at the points around the flaw. As for the results in Fig. 10 for the homogeneous case, eventhough the plastic descriptors λ_η^t and λ_η^c are monotonically increasing functions, as expected, their difference $u^{pl} = \lambda_\eta^t - \lambda_\eta^c$ is not and the plastic displacement u^{pl}, according to (37), can decrease its value. Thus, we observe that the accumulated plastic displacement change its sign according to the loading phase of the test.

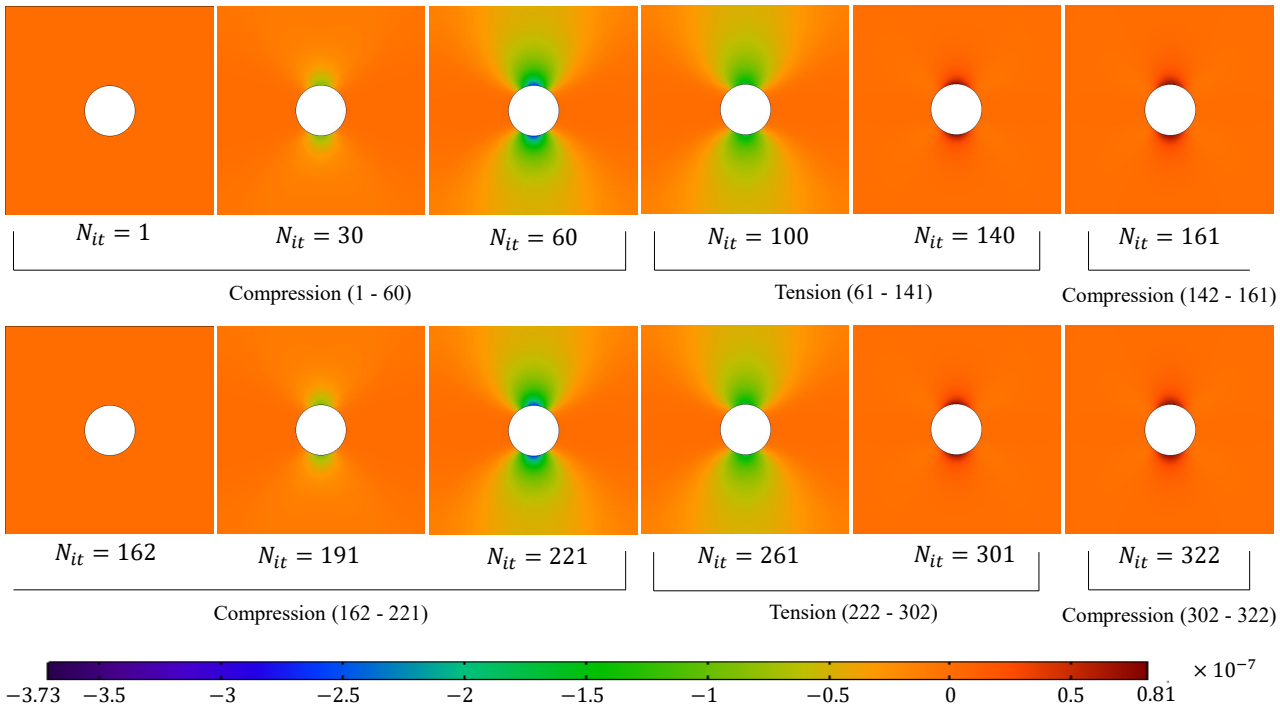

Figure 16: Non-homogeneous cyclic test. Contour plots, for different loading time steps, of the average plastic displacement $\bar{u}^{pl}$ as defined, in each point of the domain, by Eq. (75).

Figs. 17 and 18 show the contour plots of elastic and dissipated energy densities for different loading time-steps, according to the definition, respectively (27) and (44). It is worth to be noted that the elastic energy in Fig. 17 is, as expected, reversible in time and the dissipated energy in Fig. 18 is not. Moreover, concentration of elastic and dissipated energy, because of the strain gradient contribution in the elastic energy, is not concentrated in one element, but its size is due to the inter-granular distance L, that is a constitutive parameter of the problem.

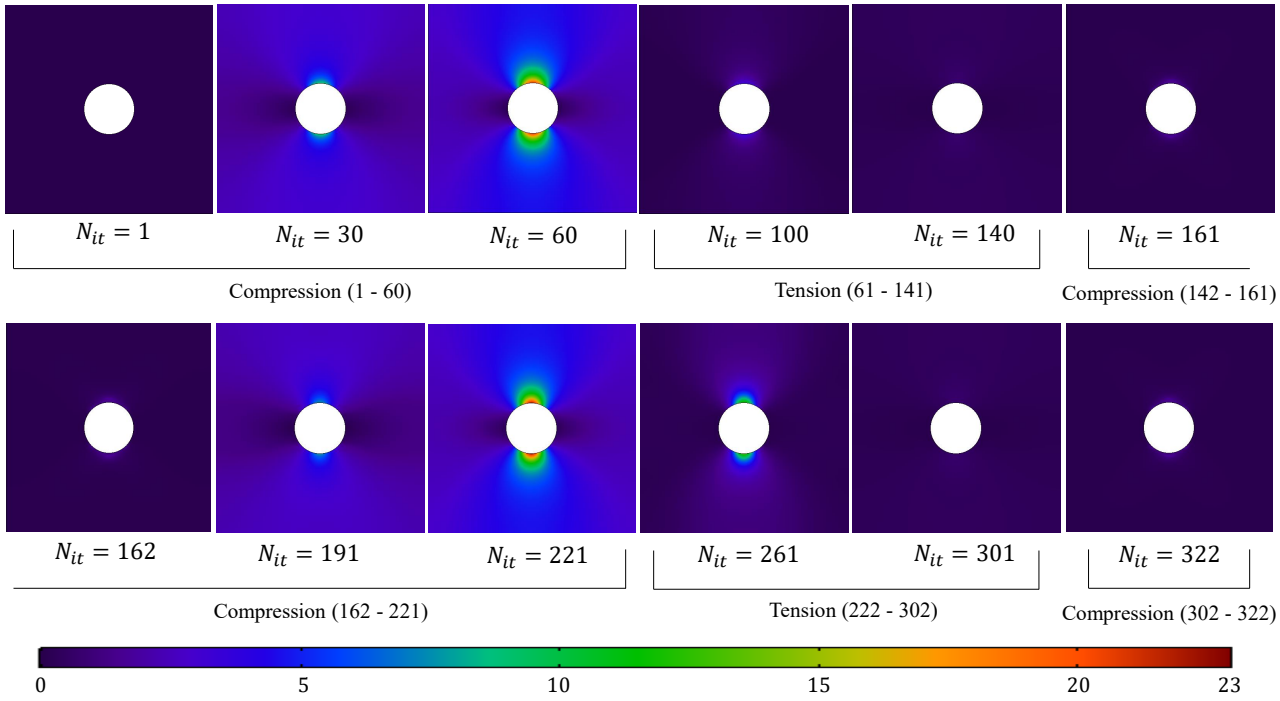

Figure 17: Non-homogeneous cyclic test. Contour plots of the elastic energy density for different loading time steps.

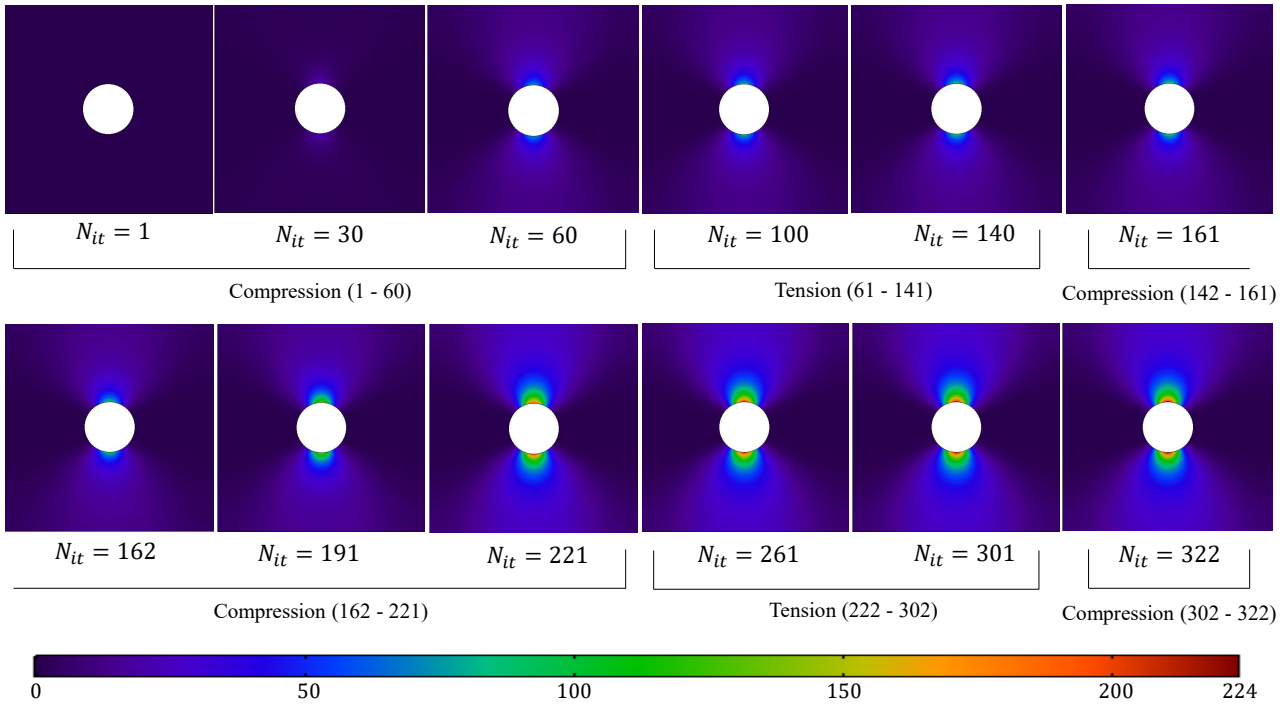

Figure 18: Non-homogeneous cyclic test. Contour plots of the dissipated energy density for different loading time steps.

Finally, in Fig. 19 we show the evolution of the load-free configuration, that is calculated, for each time step, by means of an elastic simulation of the same domain, with stiffnesses computed as in (28-33) at the current time step, by removing the external loads, and making use of a set of kinematic boundary conditions that only eliminates the rigid body motion. Clearly, in these simulations, only the pre-stress stiffness (31) and the pre-hyper stress stiffness (32) will play a role. From an experimental point of view, this shape is easy to measure and it is due to the accumulated plastic deformation.

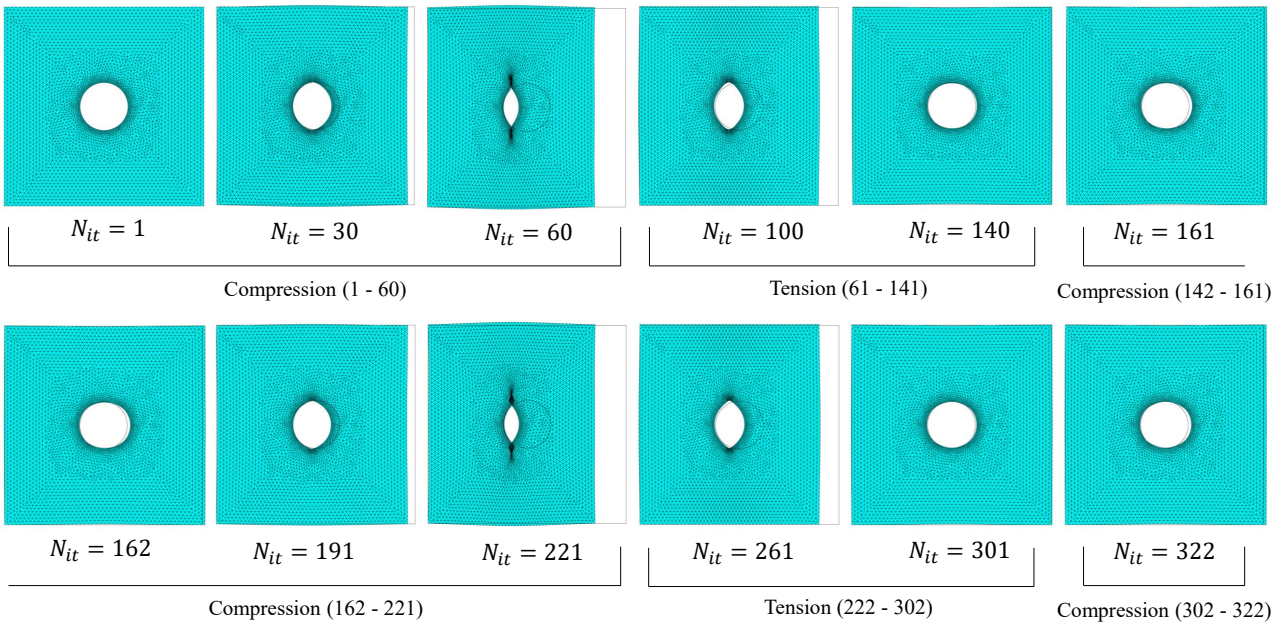

Figure 19: Non-homogeneous cyclic test. Evolution of the load-free configuration for different loading time steps. The scale factor is equal to $2.2 \cdot 10^4$.

6 Conclusion

This paper is devoted to the development of a continuum description for a special class of dissipative phenomena consisting in damage and plasticity. Strong emphasis has been put to the case of materials having granular microstructure. The present contribution extends a previous work [46], where only damage was taken into account. In the current work, we introduce plasticity by defining two independent kinematic descriptors, namely the plastic multipliers, for each position, time and grain-grain-orientation. Governing equations have been derived starting from a hemi-variational principle, from which we have derived Karush-Kuhn-Tucker (KKT) type conditions, specifying the evolution of damage and plasticity associated to each grain-grain interaction, and Euler-Lagrange equations for the objective total relative displacement.

A series of numerical simulations for homogeneous and non-homogeneous deformations shows that grain-pairs oriented in different directions have different loading histories, leading to complex anisotropic spatial patterns for damage evolution and accumulation of plastic deformation. These simulations also show the evolution of competing dissipative mechanisms, that is damage and plasticity, with loading. We observe that for certain set of parameters, plasticity can arrest growth of damage. The converse is also possible and the presented model affords the flexibility of modeling responses characterized by competing effects of damage and plasticity. For non-homogeneous deformations, every material point of the continuum evolves differently. Plasticity and damage are concentrated in vicinity of the flaw, as expected.

The key contribution of the presented model is the incorporation of simple local plastic interactions contributing to an overall complex plastic response of the material. Except for the plastic dissipation energy, there are no additional assumptions, such as flow rules, needed to specify the plastic behavior. Cyclic loading-unloading histories have been considered to elucidate the hysteretic features of the continuum, which emerge from simple grain-grain interactions. The evolution of the load-free shape has been shown not only to assess the plastic behavior, but also to make tangible

the point that, in the proposed approach, plastic strain is found to be intrinsically compatible with the existence of a placement function.

Acknowledgment

AM is supported in part by the United States National Science Foundation grant CMMI -1727433. LP is supported in part by the the RESBA project (from Politecnico di Torino).

7 Appendix: justification of normal and tangent relative displacement definitions

Let us assume that the grain p is at the origin ($\boldsymbol{X}_p = 0$) and the grain n at $\boldsymbol{X}_n = L\hat{c}$.

For the placement field indicating an elongation along the intergranular axis $\hat{c}$,

$$\chi(\boldsymbol{X}) = \boldsymbol{X} + \alpha(\boldsymbol{X}\cdot\hat{c})\,\hat{c},$$

from the one hand, the grain p does not displace ($\chi(\boldsymbol{X}_p) = 0 = u(\boldsymbol{X}_p)$), the grain n places at $\chi(\boldsymbol{X}_n) = L\hat{c} + \alpha L\hat{c}$ with a displacement $u(\boldsymbol{X}_n) = \alpha L\hat{c}$. Thus, the displacement of one grain with respect to the other along the intergranular axis $\hat{c}$ is

$$[u(\boldsymbol{X}_n) - u(\boldsymbol{X}_p)]\cdot\hat{c} = \alpha L,$$

and no relative displacement occurs in the transverse direction. From the other hand, the deformation gradient,

$$F = \nabla\boldsymbol{\chi} = I + \alpha\hat{c}\otimes\hat{c} = F^T$$

is symmetric and the objective relative displacement yields,

$$u^{np} = [I + \alpha\hat{c}\otimes\hat{c}]\,(L\hat{c} + \alpha L\hat{c}) - L\hat{c} = 2\alpha L\hat{c} + \alpha^2 L\hat{c}.$$

Thus, for small deformation the definition $(11)_1$of the normal displacement is justified, i.e. $u_\eta = \frac{1}{2}u^{np}\cdot\hat{c}$.

For the placement field indicating a shear deformation transverse (e.g. in a direction $\hat{d}$) to the intergranular axis $\hat{c}$,

$$\chi(\boldsymbol{X}) = \boldsymbol{X} + \alpha(\boldsymbol{X}\cdot\hat{c})\,\hat{d}, \qquad \hat{c}\cdot\hat{d} = 0,$$

from the one hand, the grain p does not displace ($\chi(\boldsymbol{X}_p) = u(\boldsymbol{X}_p) = 0$), the grain n places at $\chi(\boldsymbol{X}_n) = L\hat{c} + \alpha L\hat{d}$ with a displacement $u(\boldsymbol{X}_n) = \alpha L\hat{d}$. Thus, the displacement of one grain with respect to the other along the direction $\hat{d}$ orthogonal to the intergranular axis $\hat{c}$ is

$$[u(\boldsymbol{X}_n) - u(\boldsymbol{X}_p)]\cdot\hat{d} = \alpha L,$$

and no relative displacement occurs along $\hat{c}$. From the other hand, the deformation gradient

$$F = \nabla\boldsymbol{\chi} = I + \alpha\hat{d}\otimes\hat{c}$$

is not symmetric and the objective relative displacement yields,

$$u^{np} = \left[I + \alpha\hat{c}\otimes\hat{d}\right]\left(L\hat{c} + \alpha L\hat{d}\right) - L\hat{c} = L\hat{c} + \alpha L\hat{d} + \alpha\hat{c}\alpha L - L\hat{c} = \alpha L\hat{d} + \alpha^2 L\hat{c}.$$

Thus, for small deformation the definition $(11)_2$ of the tangent displacement is justified, i.e., $u_\tau = u^{np} - (u^{np}\cdot\hat{c})\,\hat{c}$.

References

[1] B.E. Abali, W.H. Müller, and F. dell'Isola. Theory and computation of higher gradient elasticity theories based on action principles. *Archive of Applied Mechanics*, pages 1–16, 2017.

[2] J-J. Alibert, A. Della Corte, I. Giorgio, and A. Battista. Extensional elastica in large deformation as\gamma-limit of a discrete 1d mechanical system. *Zeitschrift für angewandte Mathematik und Physik*, 68(2):42, 2017.

[3] M. Ambati, T. Gerasimov, and L. De Lorenzis. Phase-field modeling of ductile fracture. *Computational Mechanics*, 55(5), 2015.

[4] M. Ambati, T. Gerasimov, and L. Lorenzis. A review on phase-field models of brittle fracture and a new fast hybrid formulation. *Computational Mechanics*, 55(2), 2015.

[5] L. Ambrosio, A. Lemenant, and G. Royer-Carfagni. A variational model for plastic slip and its regularization viaγ-convergence. *Journal of Elasticity*, 110(2):1–35, 2013.

[6] H. Amor, J-J. Marigo, and C. Maurini. Regularized formulation of the variational brittle fracture with unilateral contact: numerical experiments. *Journal of the Mechanics and Physics of Solids*, 57(8):1209–1229, 2009.

[7] B. Bourdin, G. Francfort, and J-J. Marigo. Numerical experiments in revisited brittle fracture. *Journal of the Mechanics and Physics of Solids*, 48(4):797–826, 2000.

[8] B. Bourdin, G. Francfort, and J-J. Marigo. The variational approach to fracture. *Journal of elasticity*, 91(1):5–148, 2008.

[9] B. Chiaia, O. Kumpyak, L. Placidi, and V. Maksimov. Experimental analysis and modeling of two-way reinforced concrete slabs over different kinds of yielding supports under short-term dynamic loading. *Engineering Structures*, 96:88–99, 2015.

[10] L. Contrafatto, M. Cuomo, and L. Greco. Meso-scale simulation of concrete multiaxial behaviour. *European Journal of Environmental and Civil Engineering*, pages 1–16, 2016.

[11] M. Cuomo and A. Nicolosi. A poroplastic model for hygro-chemo-mechanical damage of concrete. In *EURO-C; Computational modelling of concrete structures Conference, EURO-C; Computational modelling of concrete structures*, pages 533–542, 2006.

[12] F. D'Annibale, G. Rosi, and A. Luongo. Linear stability of piezoelectric-controlled discrete mechanical systems under nonconservative positional forces. *Meccanica*, 50(3):825–839, 2015.

[13] Alessandro Della Corte, Ivan Giorgio, and Daria Scerrato. A review of recent developments in mathematical modeling of bone remodeling. *Proceedings of the Institution of Mechanical Engineers, Part H: Journal of Engineering in Medicine*, 234(3):273–281, 2020.

[14] F. Dell'Isola and L. Placidi. Variational principles are a powerful tool also for formulating field theories. In *Variational Models and Methods in Solid and Fluid Mechanics*, pages 1–15. Springer, 2011.

[15] Francesco dell'Isola and Stefano Vidoli. Continuum modelling of piezoelectromechanical truss beams: an application to vibration damping. *Archive of Applied Mechanics*, page 19, 1998.

[16] F. Freddi and G. Royer-Carfagni. Plastic flow as an energy minimization problem. numerical experiments. *Journal of Elasticity*, 1(116):53–74, 2014.

[17] M. Froli and G. Royer-Carfagni. A mechanical model for the elastic–plastic behavior of metallic bars. *International journal of solids and structures*, 37(29):3901–3918, 2000.

[18] I. Giorgio. Numerical identification procedure between a micro-cauchy model and a macro-second gradient model for planar pantographic structures. *Zeitschrift für angewandte Mathematik und Physik*, 67(4)(95), 2016.

[19] I. Giorgio, R. Grygoruk, F. dell'Isola, and D.J. Steigmann. Pattern formation in the three-dimensional deformations of fibered sheets. *Mechanics Research Communications*, 69:164–171, 2015.

[20] Ivan Giorgio, Antonio Culla, and Dionisio Del Vescovo. Multimode vibration control using several piezoelectric transducers shunted with a multiterminal network. *Archive of Applied Mechanics*, 79(9):859–879, 2009.

[21] Ivan Giorgio, Francesco dell'Isola, Ugo Andreaus, Faris Alzahrani, Tasawar Hayat, and Tomasz Lekszytcki. On mechanically driven biological stimulus for bone remodeling as a diffusive phenomenon, 2019.

[22] P. Harrison, D. Anderson, M.F. Alvarez, E. Bali, and Y. Mateos. Measuring and modelling the in-plane bending stiffness and wrinkling behaviour of engineering fabrics. *EUROMECH Colloquium 569: Multiscale Modeling of Fibrous and Textile Materials, Chatenay-Malabry*, 2016.

[23] J. Larsen, Christopher. A new variational principle for cohesive fracture and elastoplasticity. *Mechanics Research Communications*, 58:133 – 138, 2014.

[24] T.Y. Li, J-J. Marigo, D. Guilbaud, and S. Potapov. Variational approach to dynamic brittle fracture via gradient damage models. In *Applied mechanics and materials*, volume 784, pages 334–341. Trans Tech Publ, 2015.

[25] J-J. Marigo, C. Maurini, and K. Pham. An overview of the modelling of fracture by gradient damage models. *Meccanica*, 2016.

[26] Corrado Maurini, Francesco Dell'Isola, and Joël Pouget. On models of layered piezoelectric beams for passive vibration control. *Journal de Physique IV Colloque*, page 10, 2004.

[27] C. Miehe, M. Hofacker, and F. Welschinger. A phase field model for rate-independent crack propagation: Robust algorithmic implementation based on operator splits. *Computer Methods in Applied Mechanics and Engineering*, 199(45):2765–2778, 2010.

[28] A. Misra. Effect of asperity damage on shear behavior of single fracture. *Engineering Fracture Mechanics*, 69(17):1997–2014, 2002.

[29] A. Misra and P. Poorsolhjouy. Granular micromechanics model for damage and plasticity of cementitious materials based upon thermomechanics. *Mathematics and Mechanics of Solids*, page 1081286515576821, 2015.

[30] A.l Misra and V. Singh. Thermomechanics-based nonlinear rate-dependent coupled damage-plasticity granular micromechanics model. *Continuum Mechanics and Thermodynamics*, 27(4-5):787, 2015.

[31] Anil Misra, Placidi Luca, and Emilio Turco. Variational methods for discrete models of granular materials. *Encylopedia of continuum mechanics. Berlin: Springer-Verlag. Heidelberg, ISBN: 978-3-662-53605-6, doi: 10.1007/978-3-662-53605-6*, 2020.

[32] L. Placidi. A variational approach for a nonlinear 1-dimensional second gradient continuum damage model. *Continuum Mechanics and Thermodynamics*, 27(4-5):623, 2015.

[33] L. Placidi, U. Andreaus, and I. Giorgio. Identification of two-dimensional pantographic structure via a linear d4 orthotropic second gradient elastic model. *Journal of Engineering Mathematics*, pages 1–21, 2016.

[34] Luca Placidi. A variational approach for a nonlinear one-dimensional damage-elasto-plastic second-gradient continuum model. *Continuum Mechanics and Thermodynamics*, 28(1-2):119–137, 2016.

[35] Luca Placidi and Emilio Barchiesi. Energy approach to brittle fracture in strain-gradient modelling. *Proceedings of the Royal Society A: Mathematical, Physical and Engineering Sciences*, 474(2210):20170878, 2018.

[36] Luca Placidi, Emilio Barchiesi, and Anil Misra. A strain gradient variational approach to damage: a comparison with damage gradient models and numerical results. *Mathematics and Mechanics of Complex Systems*, 6(2):77–100, 2018.

[37] Luca Placidi, Anil Misra, and Emilio Barchiesi. Two-dimensional strain gradient damage modeling: a variational approach. *Zeitschrift für angewandte Mathematik und Physik*, 69(3):56, 2018.

[38] Luca Placidi, Anil Misra, and Emilio Barchiesi. Simulation results for damage with evolving microstructure and growing strain gradient moduli. *Continuum Mechanics and Thermodynamics*, 31(4):1143–1163, 2019.

[39] Payam Poorsolhjouy and Anil Misra. Effect of intermediate principal stress and loading-path on failure of cementitious materials using granular micromechanics. *International Journal of Solids and Structures*, 108:139–152, 2017.

[40] B. Reddy. The role of dissipation and defect energy in variational formulations of problems in strain-gradient plasticity. part 1: polycrystalline plasticity. *Continuum Mechanics and Thermodynamics*, 23:527–549, 2011.

[41] B. Reddy. The role of dissipation and defect energy in variational formulations of problems in strain-gradient plasticity. part 2: Single-crystal plasticity. *Continuum Mechanics and Thermodynamics*, 23:527–549, 2011.

[42] D. Scerrato, I. Giorgio, A. Della Corte, A. Madeo, N. Dowling, and F. Darve. Towards the design of an enriched concrete with enhanced dissipation performances. *Cement and Concrete Research*, 84:48–61, 2016.

[43] D. Scerrato, I. Giorgio, A. Della Corte, A. Madeo, and A. Limam. A micro-structural model for dissipation phenomena in the concrete. *International Journal for Numerical and Analytical Methods in Geomechanics*, 2015.

[44] P. Sicsic and J-J. Marigo. From gradient damage laws to griffith's theory of crack propagation. *Journal of Elasticity*, pages 1–20, 2013.

[45] M. Spagnuolo, K. Barcz, A. Pfaff, F. dell'Isola, and P. Franciosi. Qualitative pivot damage analysis in aluminum printed pantographic sheets: numerics and experiments. *Mechanics Research Communications*, 2017.

[46] Dmitry Timofeev, Emilio Barchiesi, Anil Misra, and Luca Placidi. Hemivariational continuum approach for granular solids with damage-induced anisotropy evolution. *Mathematics and Mechanics of Solids*, 2020.

[47] E. Turco, F. dell'Isola, A. Cazzani, and N.L. Rizzi. Hencky-type discrete model for pantographic structures: numerical comparison with second gradient continuum models. *Zeitschrift für angewandte Mathematik und Physik*, 67, 2016.

[48] E. Turco, M. Golaszewski, A. Cazzani, and N.L. Rizzi. Large deformations induced in planar pantographic sheets by loads applied on fibers: experimental validation of a discrete lagrangian model. *Mechanics Research Communications*, 76:51–56, 2016.

[49] E. Turco, M. Golaszewski, I. Giorgio, and F. D'Annibale. Pantographic lattices with non-orthogonal fibres: Experiments and their numerical simulations. *Composites Part B: Engineering*, 118:1–14, 2017.

[50] Y. Yang and A. Misra. Micromechanics based second gradient continuum theory for shear band modeling in cohesive granular materials following damage elasticity. *International Journal of Solids and Structures*, 49(18):2500–2514, 2012.